Photoionization Spectroscopy of Nucleobases and Analogues in the Gas Phase Using Synchrotron Radiation as Excitation Light Source

Martin Schwell and Majdi Hochlaf

Abstract We review here the photoionization and photoelectron spectroscopy of the gas phase nucleic acid bases adenine, thymine, uracil, cytosine, and guanine, as well as the three base analogues 2-hydroxyisoquinoline, 2-pyridone, and δ-valerolactam in the vacuum ultraviolet (VUV) spectral regime. The chapter focuses on experimental work performed with VUV synchrotron radiation and related ab initio quantum chemical calculations of higher excited states beyond the ionization energy. After a general part, where experimental and theoretical techniques are described in detail, key results are presented by order of growing complexity in the spectra of the molecules. Here we concentrate on (1) the accurate determination of ionization energies of isolated gas phase NABs and investigation of the vibrational structure of involved ionic states, including their mutual vibronic couplings, (2) the treatment of tautomerism after photoionization, in competition with other intramolecular processes, (3) the study of fragmentation of these molecular systems at low and high internal energies, and (4) the study of the evolution of the covalent character of hydrogen bonding upon substitution, i.e., examination of electronic effects (acceptor, donor, etc.).

Keywords Electronic spectroscopy · Nucleobase analogues · Nucleobases · VUV photophysics · VUV spectroscopy · VUV synchrotron radiation

M. Schwell (✉)
Laboratoire Interuniversitaire des Systèmes Atmosphériques (LISA), UMR 7583 CNRS, Universités Paris-Est Créteil et Paris Diderot, Institut Pierre et Simon Laplace, 61 Avenue du Général de Gaulle, 94010 Créteil, France
e-mail: martin.schwell@lisa.u-pec.fr

M. Hochlaf
Laboratoire Modélisation et Simulation Multi Echelle, Université Paris-Est, MSME UMR 8208 CNRS, 5 bd Descartes, 77454 Champs-sur-Marne, France

Contents

Abbreviations

AE	Appearance energy
AIE	Adiabatic ionization energy
EI	Electron impact ionization
FEL	Free electron laser
IE	Ionization energy
NAB	Nucleic acid base
PE	Photoelectron
PES	Photoelectron spectroscopy
PI	Photoion
PIE	Photoionization efficiency
PIMS	Photoionization mass spectrometry
SPES	Slow photoelectron spectrum
SPI	Single photon ionization
SR	Synchrotron radiation
TOF	Time-of-flight
TPEPICO	Threshold photoelectron photoion coincidence
TPES	Threshold photoelectron spectroscopy
VIE	Vertical ionization energy
VUV	Vacuum ultraviolet

1 Introduction

The study of large biomolecules, such as DNA and RNA, requires prior and extensive knowledge of the physicochemical properties of their smaller building blocks, for example, nucleobases and nucleosides. In particular, the investigation of ionized species of DNA or RNA has gained in importance during the last decades, because the damage produced by the interaction between ionizing radiation and
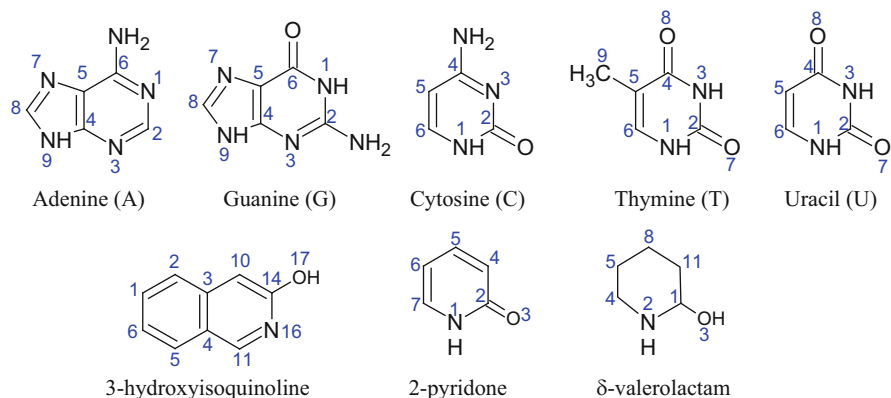
Scheme 1 Chemical structures of the nucleic acid bases (with standard atom numbering) and three NAB analogues (with common numbering used in the literature, for non-H atoms only). The photoionization spectroscopy of these molecules is presented in this chapter

biological matter leads, for instance, to hazardous genetic mutations, potentially mediated by ions, with enhanced risk for cancer [1–3]. The mechanisms underlying DNA or RNA lesions are still under study and require the precise determination of thermochemical data and properties of the reactive species such as their ionization energy (IE), their spectroscopy, their nuclear dynamics, and a comprehensive understanding of their electronic structure. At the atomic level, a deep interpretation of induced radiation effects on the genetic material seems crucial with the growing development of cancer treatments by irradiation therapy. Since the electronic structure of DNA and RNA bases is complex, the comparison of their spectra to those of their analogues helps our understanding of the intrinsic processes occurring when these biologically relevant molecules are ionized and on the damage created when they are struck by ionizing radiation. Here we will indeed show how the complexity of the spectra increases gradually from 3-hydroxyisoquinoline (3-HQ) to 2-pyridone/2-hydroxypyridine, to δ-valerolactam, to thymine (T)/uracil (U), to adenine (A), to cytosine (C), and finally to guanine (G). In Scheme 1 we present the chemical structures of the nucleic acid bases (denoted hereafter as NABs) and three of their analogues whose photoionization spectroscopy will be presented in this chapter.

The question is why is complexity increasing? In fact, growing complexity is not linked to the skeletal structure of the molecules but rather it originates from the number of tautomers/rotamers and conformers that can be present in their neutral and ionic forms. Indeed, considering the analogues, 3-HQ presents a unique tautomeric form in the gas phase (the lactim) whereas, upon photoionization, two tautomeric cations (lactim$^+$/lactam$^+$) can be formed for 2-pyridone. For δ-valerolactam the situation is more complicated in spite of its simpler structure (cf. Scheme 1). For this base analogue we can count two tautomers, several conformers (boat/chair) and rotamers (*cis/trans*) which complicates matters

considerably, for example, the theoretical treatment of its VUV spectroscopy as depicted below. In this context, the case of guanine is particularly interesting and challenging to treat since the guanine cation is predicted to possess 36 tautomers/conformers lying close in energy. So how do these features influence the spectroscopy and the photoionization mechanisms of these species? The answer to this question may help to enlighten the still not well understood stability of DNA bases upon UV/VUV irradiation.

NABs are important building blocks of life. Therefore, their possible chemical genesis and survival, for example in an early Earth environment (or other "extreme" environments), has motivated many studies on the prebiotic formation and UV photophysics of these species. They were performed in the context of the study of the origin of life. It should be noted that these so-called astrobiological aspects of NAB photoionization and fragmentation are not the focus of the present chapter.

From the experimental point of view, photoion (PI) and photoelectron (PE) spectroscopies are powerful techniques for studying intramolecular photodynamics beyond the ionization energy. They have been extensively employed to study the single photoionization (SPI) of molecules that can be vaporized relatively easily. In order to ionize a molecule in the valence shell with a single photon, the wavelength of the photon falls generally in the vacuum ultraviolet (VUV) spectral domain. VUV radiation is roughly situated between 200 and 50 nm ($6.2 \text{ eV} < E_{photon} < 24.8 \text{ eV}$). It does not propagate in air due to the Schumann–Runge band transitions (between 200 and 170 nm) of molecular oxygen. In addition, lasers can be used as a light source in the VUV spectral domain in order to study photoinduced phenomena by SPI. Current advances are in very high resolution (sub-wavenumber). PI and PE spectroscopies using tunable VUV laser radiation generated by resonant four-wave mixing have been reviewed very recently by Ng [4]. Such experimental setups are costly since several lasers are needed for the photon mixing. Moreover, their proper alignment is an experimental challenge and is routinely performed in only a few laboratories in the world. Nucleobases have not been studied so far by SPI with tunable VUV lasers. Synchrotron radiation (SR), on the other hand, has been widely used as a light source in order to explore higher excited states in the VUV region, together with PI/PE spectroscopy. Recently, Qi and co-workers reviewed advances of VUV-SR photoionization mass spectrometry with particular attention to non-volatile molecules [5, 6]. Electron spectrometers are also operated routinely in connection with VUV-SR beamlines. They mainly work in the electron/ion coincidence regime and the most sophisticated ones also employ particle imaging techniques [7, 8]. SR offers a broad and continuous tunability which is its main advantage as compared to laser sources or VUV discharge lamps. Furthermore, at third generation synchrotron light sources, which are routinely operated today all over the world, the brilliance typically exceeds 10^{18} photons/s/mm^2/mrad^2/10^{-3}BW (where BW is the bandwidth around the light frequency), thus permitting the study of very small quantities.

With the advent of efficient vaporization techniques, such as laser desorption or nanoparticle desorption, photoionization and photoelectron spectroscopy were

applied to molecules that have very low vapor pressures at room temperature. Furthermore, enhancements of the sensitivity of detectors and of the efficiency of ion/electron collectors have led to the possibility of working with very small quantities inside the ion source. Consequently, even thermal vaporization of macroscopic samples in combination with effusive inlets or supersonic expansions can nowadays be used for the study of non-volatile (bio-) molecules by sophisticated gas phase spectroscopic methods. This is especially true for isolated nucleobases which possess a certain thermal stability in comparison with other, more fragile biomolecules (e.g., amino acids or peptides). In our opinion, the most notable examples of state-of-the-art VUV-SR spectroscopy applied to NABs and other related non-volatile biomolecules are found in [9–14].

The main objectives of the studies reviewed in this chapter are (1) accurate determination of ionization energies of isolated gas phase NABs and investigation of the vibrational structure of involved ionic states including their mutual vibronic couplings, (2) treatment of tautomerism after photoionization, in competition with other intramolecular processes, (3) study of fragmentation of these molecular systems at low and high internal energies, and (4) study of the evolution of the covalent character of hydrogen bonding upon substitution, i.e., examination of electronic effects (acceptor, donor, etc.).

The chapter is divided as follows: In Sect. 2, we detail the different experimental methodologies for studying the photoionization spectroscopy of NABs. In Sect. 3, we describe the quantum chemical methods used to analyze NABs photoionization and photoelectron spectra. Finally, in Sect. 4, we present key results of specific molecules.

2 Experimental Methodologies to Measure Photoionization and Photoelectron Spectra of NABs

2.1 Earlier Photoelectron (PE) Spectroscopy Experiments

HeI PE spectra of NABs have been measured since the mid-1970s by several groups [15–21]. One should note the high quality of the early pioneering experimental research, often carried out in combination with theoretical calculations. For example, using a commercial Perkin–Elmer photoelectron spectrometer and HeI emission at 21.21 eV, a spectral resolution down to 20–25 meV could be attained in the work of Dougherty et al. [16]. However, little evidence of vibrational structure could be revealed in these spectra. Only in the mid-2000s were these spectra interpreted in depth theoretically, including spectral intensity calculations [22–24]. In the 1990s, the zero kinetic energy electron (ZEKE) photoelectron spectroscopy technique was introduced and developed [25]. This technique is capable of recording PE spectra with spectral resolutions well below 1 meV, in the vicinity of the ionization threshold, by means of resonance enhanced

multiphoton ionization (REMPI) schemes and using lasers. Later on, REMPI (and also Laser Induced Fluorescence (LiF)) spectroscopy was widely used to measure high resolution optical spectra of NABs in the mid-UV where the intense $S_n \leftarrow S_0$ transitions are located (see the chapter by deVries et al.). However, it is difficult to apply REMPI to explore the photodynamics of higher excited states located well beyond the ionization energy. For those states, SPI with VUV synchrotron radiation or VUV lasers are favorably used.

2.2   Electron Impact Ionization Measurements on NABs

For the sake of completeness, we give here a short overview of experiments where electron impact ionization (EI) is used, generally in combination with mass spectrometry, to explore the photoion spectroscopy and dynamics of dissociative ionization beyond the ionization energy. We note that electron impact is a process which is physically completely different from photoabsorption (the latter process is sometimes called "photon impact", a term that might be misleading). The energetics of electron impact ionization can be well analyzed by energy and momentum conservation of the multiple interacting particles, whereas photoabsorption is a process where the photon energy is completely transferred to the molecule with the photon being annihilated. In earlier studies of dissociative ionization, it was found that the energy transferred to a molecule by electrons having 70 eV kinetic energy is grossly equivalent to photoabsorption of 35 eV photons [26]. We also note that photoionization cross sections are significantly greater than the EI ionization cross sections when incident electrons have a kinetic energy close to the photon quantum energy. In addition, the relative intensities of the bands by electron impact are different from those measured by photon impact because of different selection rules upon ionization. For instance, different threshold functions are measured and are widely used in the literature to deduce ionization energies from the corresponding spectra.

The kinetic energy of the impacting electrons can be scanned easily by changing the accelerating electric field of the electron source of the mass spectrometer. We note, however, that the experimental error of ionization and appearance energies is generally of the order of 0.2 eV and very often systematic errors are found when comparing threshold values measured by EI to those measured by photoionization using synchrotron radiation, for example. This is probably due to the accurate energy scale calibration using photon excitation where resonant transitions of rare gas absorption lines are used for that purpose. To our knowledge, the first EI mass spectra of NABs and their derivatives were recorded in 1965 by Rice et al. [27, 28], followed by others [29–32]. More recently, Denifl et al. used a hemispherical electron monochromator to study the threshold electron impact ionization of uracil and two of its chlorine derivatives [33, 34]. These authors measured the vertical ionization energy of uracil, found at 9.59 eV, with a precision of 0.08 eV. They also showed that the energy spread of the impinging electrons can be reduced to 35 meV

using such a monochromator, which is quite promising. We also mention that electron impact ionization has been used in experiments on NABs where the collisionally activated dissociation and gas phase tautomerization of NAB radical cations has been investigated [35, 36], in combination with extensive ab initio calculations.

2.3 Synchrotron Radiation (SR) as an Exciting Light Source

During the last decade, many excellent VUV-SR studies on gas phase nucleobases and related molecules were performed (see for example [9, 11–13, 37–45]). Generally, the white synchrotron light is monochromatized using normal incidence monochromators (NIM). In principle, the undulator of a synchrotron beamline can be used alone as a scanning device. In such experiments, the NIM grating would be set to its zero order, transmitting the maximum of number of photons without diffraction. The emission of VUV undulators has typical bandwidths of the order of 0.2–0.5 eV, which naturally limits the bandwidth of such spectra.

Since the density of the target molecules inside the ion source is usually very low for experiments with NABs, gratings with low groove numbers, which allow the transmission of more photons, are employed. Among them, the 200 g/mm grating integrated in the 6.65 m NIM at the undulator beamline DESIRS of the French SOLEIL synchrotron facility is used for such "flux-hungry" applications. Typical VUV bandwidths of the PI and PE spectra are on the order of 5–30 meV. Such spectral resolutions can be considered as state-of-the-art for VUV-SR experiments on NABs. Smaller bandwidths, below 1 meV, for example, can easily be achieved in principle with the current synchrotron-based PI and PE spectrometers. Nevertheless, the density of the target molecules would have to be further enhanced beyond what is possible today with current vaporization techniques. Furthermore, spectra of complex biomolecules could be congested and/or complicated by co-existing tautomers (or rotamers), so that high resolution spectrometers are not often of essential use.

From a perspective point of view, free electron lasers (FEL) operating in the VUV spectral regime will become more and more available in the near future. Such pulsed light sources should allow for pump-probe spectroscopy and thus the photodynamics of higher excited states could be studied directly using two synchronized VUV light pulses, combining, for example, FEL and VUV laser radiation. Moreover, FEL devices will have much higher brilliances compared to third generation SR sources (up to 10^{21} photons/s/mm^2/mrad^2/10^{-3}BW or even more). Thus, smaller sample quantities can be used. Further experimental developments are, however, needed because (1) these light sources are generally pulsed and their tunability is limited and (2) it is difficult to conduct electron/ion coincidence experiments (see below) with these FEL VUV light sources.

2.3.1 Vaporization Methods

At ambient pressure and temperature, NABs are solids with low vapor pressures. The sample can be placed directly in the ion source if the latter is completely heatable [37]. Nevertheless, most of the studies cited above have been conducted by heating the solid NAB sample in an oven prior to supersonic expansion into a molecular beam. Effusive inlets have also been used. Generally, macroscopic NAB samples have to be heated to about 130–250°C for a typical PI or PE spectroscopic experiment. The exact temperature needed for vaporization depends on the specific compound and on the sensitivity of the instrument used for PE and/or PI detection. The vapor pressure increases exponentially with temperature, and thus a few degrees more in the vaporization source can lead to a significant gain in signal-to-noise ratio. Eventually, thermal degradation may occur that is revealed easily in the mass spectrum by the presence of TOF peaks corresponding to CO_2, and/or other small, thermodynamically stable species (such as HCN or NH_3) eliminated upon pyrolysis. Whether a certain ion is indeed a parent ion formed by ionization of a pyrolysis product or a fragment formed by dissociation ionization of the parent NAB can generally be verified by measuring its appearance energy.

The technique of thermal vaporization of nanoparticles is applied to soft vaporization of NABs. Nowadays, such aerosol sources are operated routinely at the SOLEIL synchrotron (Saint Aubin, France) [10] and at the Advanced Light Source (Berkeley, USA) [45]. We show the experimental setup of the aerosol source operated at the DESIRS beamline at SOLEIL in Fig. 1. This technique has been shown to be a softer method of vaporization than simple heating of macroscopic samples [11]. Originally it was developed by the atmospheric physics community. In 2005 it was introduced at synchrotron beamlines by Mysak et al. [46]. Aerosol vaporization has been shown to work particularly well for amino acids which are more easily subject to thermal degradation upon heating than NABs [10, 47]. Within this method, an aqueous (or ethanolic) solution of approximately 1 g/L of the biological compound is nebulized, yielding a cloud of micrometer-sized droplets which are then dried efficiently by a diffusion dryer. The resulting nanoparticles, which consist chemically of the pure substance to be studied, are spatially focalized using an aerodynamic lens system providing a beam of nanoparticles with sub-millimeter dimensions and very low divergence. This beam is directed onto a hot tip where the nanoparticles are vaporized yielding a tiny vapor plume ideal for interfacing with a brilliant light beam. The source is continuous and, using a constant output atomizer (TSI) for nebulization, the density of the target molecules inside the ion source is stable for several hours. Consequently, spectroscopic studies can be performed.

Another notable advantage of the aerosol vaporization technique concerns the relatively low rate of sample consumption in a typical PE/PI spectroscopic experiment. Indeed, this rate is reduced by a factor of ~20 as compared to simple oven vaporization [11]. It can thus be an interesting alternative when samples are costly
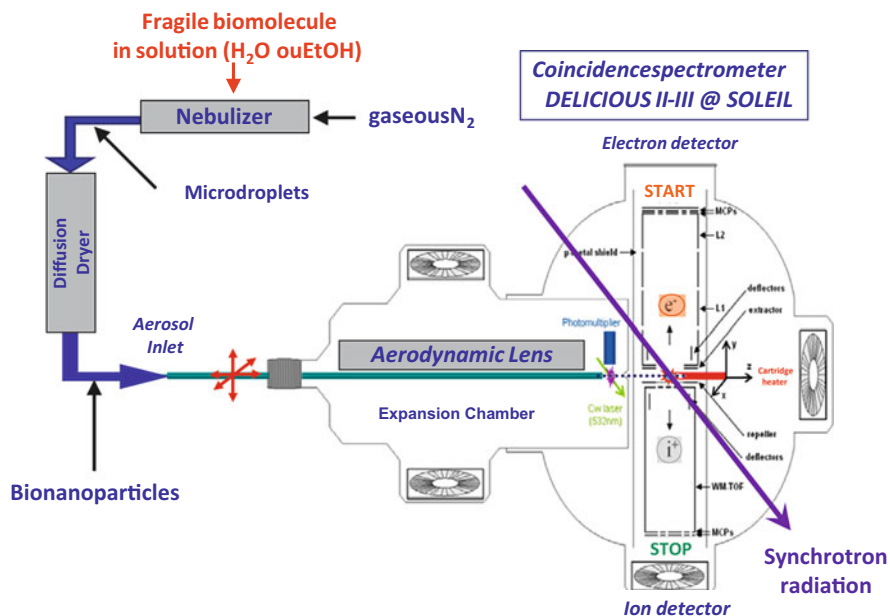
Fig. 1 Thermal vaporization of bionanoparticles connected to coincidence photoelectron and photoion spectroscopy. These particles are produced by nebulization of an aqueous solution of the biomolecule and subsequent drying of the microdroplets. The nanoparticles, consisting of the pure biological compound to be studied, are spatially focused through an aerodynamic lens system. They impinge on a cartridge heater creating tiny vapor plumes ideal to be interfaced with brilliant SR. These kinds of aerosol sources for soft vaporization are operated today at the SOLEIL synchrotron and at the Advanced Light Source

or available only in very small quantities. A shortcoming is that the gas phase neutrals are formed at higher temperatures as compared to jet-cooled molecules.

Very recently, pulsed laser desorption was successfully used in combination with tunable (and continuous) VUV-SR, although the duty cycle of laser/synchrotron light interaction is unfavorable [5, 6, 48]. In these challenging experiments, the desorption and ionization processes are separated in space (and thus in time, since the desorbed molecules need to travel to the center of the ion source). The results are very encouraging. For example, Zhou et al. [6] succeeded in measuring PI mass spectra of the nucleoside uridine with a good signal-to-noise ratio at several photon energies close to the ionization threshold. Prior to ionization, the uridine molecules are desorbed using the fundamental emission of a nanosecond Nd:YAG laser at $\lambda = 1{,}064$ nm and operating at a repetition rate of 10 Hz. The focused laser beam hits the solid sample which is placed on a substrate located at variable distances, ranging from 1–4 mm, from the center of the ion source. The power density of the laser pulse is of the order of 10^7 W $\cdot$ cm^{-2} (power per unit of irradiated area). In each period between the laser pulses, ions formed by VUV-SR ionization of desorbed neutrals were collected by a home-made reflectron time-of-flight mass spectrometer

at the much higher repetition rate of 10 kHz. Using this technique, Zhou et al. also presented photoionization efficiency (PIE) spectra for the amino acid α-alanine.

The experimental approach of Kostko et al. [48] is quite different from that of Zhou et al. [6]. Indeed, Kostko et al. used an Nd:YLF laser emitting at $\lambda = 349$ nm and operating at a repetition rate of 2.5 kHz for desorption. This laser radiation is directed into a modified commercial time-of-flight secondary ion mass spectrometer (ToF-SIMS), which is commonly employed for mass spectrometric imaging experiments. This kind of mass spectrometer is normally operated using ion sputtering with fast, pulsed ion beams of nanosecond duration and several keV kinetic energy. Kostko et al. [48] were thus able to measure PI mass spectra of A, T, C, and U NABs. In their work, the laser desorption dynamics are studied and it is found that the internal temperature of laser-desorbed thymine is about 800 K whereas its translational temperature is well below, ranging from 216 to 346 K for the four NABs under study. Furthermore, the translational temperatures decrease with increasing laser power density (from 10^8 to 4.5×10^8 W·cm^{-2}) which is deduced from the measurement and exploitation of the shape of the TOF mass peaks. As an explanation, these authors suggested efficient collisional cooling during the laser desorption process. Increasing the laser power leads in fact to the vaporization of more molecules per unit of surface area and thus the number of collisions is enhanced, leading to translational cooling. This effect is similar to the enhanced cooling in molecular beam experiments which is observed upon increasing the stagnation pressure.

More generally, we note that each vaporization method leads to different internal and translational energies of the produced parent and fragment cations. This aspect has been studied in depth in [10, 46–48] and the literature cited therein. The amount of internal energy E_{int} imparted to the neutral upon vaporization is important to know for gas phase electronic spectroscopic studies of large molecules like NABs, since it directly affects their tautomer/conformer/rotamer distribution. The ionization energy cannot be used to get an estimate of E_{int} since it is well known that the IE is not much affected by the temperature of the neutral molecule that undergoes photoionization. In rare cases, hot bands are observed below the experimental adiabatic ionization energy (AIE) but in many cases Franck–Condon factors are unfavorable for the appearance of such bands. In contrast, the appearance energies (AE) of fragments formed by dissociative photoionization are very much affected by the temperature of the parent neutral. In an "Arrhenius-like" behavior, the amount of internal energy can be deduced totally from the activation barrier, leading to a red shift of the AE that can be easily observed. For example, in the work of Gaie-Levrel et al. [10], a red shift of 0.57 ± 0.1 eV is observed for the formation of m/z 130 from the dissociative photoionization of tryptophan when raising the temperature of the hot finger, used for the aerosol vaporization, from 423 to 558 K. An observed AE red shift can in turn be used to deduce E_{int} by assuming that the latter is approximated by a collection of harmonic oscillators, as has been done in [47, 48]. In this context, one has to calculate vibrational frequencies of the molecule by theoretical chemistry methods. Consequently, this effect can be used in a straightforward manner to study the energy transfer during

vaporization with a particular method, by using VUV photoionization with tunable SR. Since tautomers, conformers, and rotamers produce in most cases the same fragment, the red shift is not affected by their distribution.

2.3.2 Spectroscopic Methods

Photoionization Mass Spectrometry (PIMS)

The first study of the photoionization of NABs, which combines VUV-SR with (quadrupole) mass spectrometry, was performed by Jochims et al. [37] on A, T, and U at the BESSY II synchrotron (Berlin). The spectral domain covered in this work was 6–22 eV and the measuring interval was 25 meV. The macroscopic neutral samples were placed and vaporized inside the heatable ion source. Ionization energies (IEs) of the NABs photoion parent and the appearance energies (AEs) of their photofragment cations were determined with accuracies ranging from 0.03 to 0.1 eV. The dissociative ionization pathways were discussed in depth using useful thermodynamical data from the literature (see also below). Astrophysical implications concerning the prospects and survival of NABs in interstellar media and meteorites were also discussed. We note here that IEs and AEs measured in this work must be considered as upper limits. To this end, experiments using threshold electrons (i.e., electrons with close to zero kinetic energy) are more powerful in determining more accurate IEs, AEs, and enthalpies of formation of the corresponding cations (see below). In principle, the thermal energy content of the parent neutral has to be subtracted from the measured IEs and AEs. On the other hand, activation barriers of photodissociation reactions often lead to the measurement of too-high AEs. These two effects might cancel out for simple single bond rupture reactions. In addition, a fragment AE can be subject to a substantial kinetic shift, ΔE_{kin} since at threshold, the reaction might be too slow to be observed. These effects were discussed in more detail by Schwell and co-workers in [49, 50]. Such kinetic shifts can be estimated by statistical models based on the possible existence of a transition state along the reactive pathways (see for example [51]).

In the last decade, PIMS was widely used at the Chemical Dynamics beamline at the Advanced Light Source to study jet-cooled NABs. The use of molecular beams in these experiments enabled the study of small, homogeneous, and heterogeneous NAB clusters. For instance, Belau et al. [38] investigated the microhydration of A, T, G, and C by recording PIE curves in the 7.9–10.5 eV incident photon spectral domain. The typical scanning step of these PIE spectra was 50 meV. The authors mainly found that ionization energies of mixed NAB-$(H_2O)_n$ ($n = 1$–3) clusters decrease by ~0.3 eV when going from $n = 0$ to $n = 3$, except for guanine (see below). Later on, the same group studied proton transfer inside homogeneous and heterogeneous NAB clusters using PIMS in combination with electronic structure calculations on the shape of the potential energy surface along the reaction coordinate [13, 45]. NAB dimers have also been studied in depth using PIMS experiments complemented with extensive quantum-chemical calculations [12],

where the effects of π-stacking, H-bonding, and electrostatic interaction between the cluster forming molecules were deeply investigated.

Electron/Ion Coincidence Spectroscopy and Imaging Techniques

This approach is currently pursued at the DESIRS beamline at the SOLEIL synchrotron. It concerns the use of electron/ion coincidence spectroscopy and particle imaging techniques in order to explore the photodynamics beyond the ionization energy of biological relevant molecules. The most recent instrument is called DELICIOUS III. It consists of a multipurpose double imaging particle coincidence spectrometer [8]. This spectrometer offers the possibility to analyze kinetic energies of coincident electrons and ions simultaneously and opens up the possibility to do state-selective threshold experiments, such as Threshold Photoelectron Spectroscopy (TPES) and Threshold Photoelectron and Photoion Coincidence (TPEPICO) spectroscopy with sub-meV resolution. In a typical experiment, the VUV photon energy is scanned and the electrons and ions formed are detected in coincidence. Typical count rates are on the order of 10^4 per second for the electrons and 10^3 for the ions. At the same time, the kinetic energy of the photoelectrons formed is analyzed using velocity map imaging. In a TPES spectrum, close to zero kinetic energy photoelectrons are plotted against the photon excitation energy. In a TPEPICO spectrum, the parent (or fragment) ion is detected in coincidence with zero kinetic energy photoelectrons. The coincidence counts are plotted against photon energy. In DELICIOUS III, an ion imaging is also performed, where the photoelectron images are correlated both to the mass and the ion kinetic energy and recoil directions. Among its attractive capabilities, this apparatus allows one to assess the electron spectroscopy of mass-selected species. We note that mass selection does not necessarily mean *species*-selective since in an ordinary mass spectrum a given mass can be either a fragment or a parent ion.

As discussed above, it is difficult to perform TPES or TPEPICO spectroscopy of NABs with very high resolution. This is mainly because of the low density of target molecules inside the ion source. Very recently, Hochlaf, Poisson and co-workers [9, 52] proposed an ingenious alternative where the photoelectrons are allowed to possess kinetic energies up to a certain value (e.g., 75 meV) in order to increase the signal-to-noise ratio of the spectrum. This technique is called "Slow Photoelectron Spectroscopy (SPES)." Basically, a SPES spectrum is very similar to a TPES spectrum. For instance, it permitted the measurement of the photoelectron spectrum of 2-pyridone, a model molecule for DNA nucleobases, with 9 meV resolution [9]. This allowed the resolution of the vibrational structure of the two co-existing tautomers of this molecule. In 2013, TPEPICO spectra of adenine and cytosine have been reported, with 40 meV spectral resolution, from 8 to 11 eV [11]. These experimental results are detailed below.

We note that a double imaging electron/ion coincidence spectrometer is also implemented at the VUV bending magnet beamline of the Swiss Light Source

(Villigen) [7]. However, biomolecules are not in the scientific focus of experiments performed at this beamline so far.

3 Theoretical Methods for the Analysis of Photoionization and Photoelectron Spectra

The full understanding of the photoionization reaction

$$M + h\nu \rightarrow M^* \rightarrow M^+ + e^- \rightarrow \text{fragments}$$

needs characterization of the neutral species (M), the intermediate (an electronically excited molecule, M*), the cation (M$^+$), and the fragments (neutral and cationic). During the first steps of this mechanism, the Franck–Condon principle is a priori in action. Since these species can be either closed or open shell molecular systems, we should use theoretical approaches that can describe both of them. In addition, their wavefunctions may be mono- or multiconfigurational in nature. To reach the so-called chemical accuracy, large computations should be performed. Such accurate theoretical calculations are of enormous help for assigning experimental spectra and for understanding the physico-chemical processes occurring after interaction of VUV light with NABs or their analogues. This concerns identification of the equilibrium structures of the neutral and cationic parent species and of their fragments, the pattern of their electronic states, the shape of their potential energy surfaces, fragmentation pathways, etc. In this section we review recent techniques applied for these purposes. Nowadays, most of these techniques are standard. They are implemented in several commercial ab initio quantum chemistry packages, e.g., Gaussian [53], Molpro (MOLPRO is a package of ab initio programs written by [54]), Molcas [55], Gamess [56], Turbomole [57], Columbus [58], and Aces II [59].

For monoconfigurational molecular systems, Hartree–Fock, conventional many-body [60], perturbation theory (Møller Plesset, MP2, MP4, . . .) [61, 62, and references therein; 63], coupled cluster approaches [64–66], and density functional theory based methods [67, 68] can be used. In 2000, Barone and co-workers [69] developed a hybrid Hartree–Fock/density functional model to optimize the equilibrium geometries of NABs and their radical cations. The computed structures and energetics (e.g., ionization energies) are in good agreement with available experimental data. This validated the use of their approach for the investigation of such open shell systems. These authors showed how this technique can be used for the assignment of experimental fragmentation mass spectra. Higher quality theoretical data can be obtained by coupled clusters approaches with perturbative treatment of triple excitations (RCCSD(T)) [64], which are, however, computationally demanding. Very recently, the use of newly implemented explicitly correlated methodologies [70–72], in addition to the inclusion of core-valence and scalar-relativistic

corrections, allowed accurate determination of ionization energies (IEs) of small and medium sized molecular systems such as NABs and analogues. Indeed, the differences between the calculated and the measured IEs are less than 1 meV. For such large sized molecular systems, these computations become feasible because of the reduction of CPU time and disk space by up to two orders of magnitude when using (R)CCSD(T)-F12 instead of (R)CCSD(T) for similar accuracy [73–76]. For explicitly correlated calculations, Peterson and co-workers developed an ensemble of explicitly correlated basis sets (cc-pVXZ-F12, X=D,T,Q)) to describe first and second raw atoms [77], in connection with their corresponding auxiliary basis sets and density fitting functions [78–81]. The core-valence effects are evaluated as the difference between electronic energies with only valence electrons correlated and electronic energies with all electrons correlated (e.g., at the (R)CCSD(T)/ cc-pwCVTZ level of theory [82, 83]). The scalar-relativistic energetic contributions correspond to the difference between electronic energies at the (R)CCSD(T) level where the atoms are described by Dunning's basis sets [84] without using the spin-free, one-electron Douglas–Kroll–Hess (DKH) Hamiltonian [85, 86] and at the (R) CCSD(T) level in connection with cc-pVXZ-DK basis sets [87] with the DKH Hamiltonian.

For multiconfigurational wavefunctions, configuration interaction techniques, such as multiconfiguration self-consistent field (MCSCF) and its variant, the complete active space self-consistent field (CASSCF) [88, 89] and the costly internally contracted multireference configuration interaction (MRCI) [90, 91] approaches are widely used. For NABs and their analogues, the choice of the CASSCF active space is not trivial, due to the computational hardware limitation. The best active space is chosen as a compromise between computational time and accuracy, where several tests should be performed to determine the appropriate size of active space without significant change in the order of electronic states of the NABs or analogues. Taking into account the size of the molecules under analysis, the good compromise (computational cost vs accuracy) corresponds to the inclusion of all molecular orbitals (MOs) from HOMO-n to LUMO+m where n and m equal 2–3 (cf. [92–98]). The lowest MOs are kept frozen. The CASSCF vectors are hence constructed using all configuration state functions (CSFs) obtained after excitations of all active electrons in these orbitals. This results in several thousands of CSFs to be treated. At the MRCI level only the configurations of the CASSCF wavefunction with coefficient modulus larger than a threshold (of 0.0–0.2) are included in the reference vector. The MRCI active space is constructed after single and double excitations of active electrons from the reference space into the virtual MOs. This usually results in more than ten million uncontracted configurations having to be considered. For better accuracy we generally quote the energies including the Davidson correction (MRCI+Q) that accounts for the contribution of higher order electron excitations [99]. Alternatively, one may perform multistate complete active space second-order perturbation theory (MS-CASPT2) [100] or CIPT2 [101] to consider dynamical electron correlation instead of the costly MRCI. In the MS-CASPT2 method the gradients are implemented [102]. Hence, this method may be used for the multidimensional mapping of the potential energy surfaces of

the neutral and the ionic electronic states close to and far from the molecular region, for instance for electronic excited states geometry optimizations, reaction pathways identifications, and computation of non-adiabatic transition characterizations, as illustrated in [103, 104].

For the investigation of the electronic excited states of ionized NABs, multiconfigurational techniques remain the methods of choice. Nevertheless, they are computationally demanding. In cases where the corresponding electronic wavefunctions are dominantly described by a unique determinant, time-dependent density functional theory (TD-DFT) [105, 106], equation-of-motion coupled clusters (EOM-CC), and third-order algebraic-diagrammatic construction approximation scheme (ADC(3)) for the one particle Green's function [107–109] all represent good approximations. Through a comparative study of the lowest electronic states of the 2-pyridone$^+$ cation (a NAB analog) using PBE0/6-311 + G(d,p) and CASSCF/MRCI/cc-pVDZ, Hammoutène et al. [94] showed that both TD-DFT and CASSCF/MRCI describe correctly the vertical excitation energies of these electronic states, whereas one should use multiconfiguration methods for mapping the evolution of the potential energy surfaces far from the molecular region and for treating the unimolecular decomposition processes undertaken by the 2-pyridone$^+$ cation. This is due to the possible change of the nature of the wavefunctions of these electronic states along the corresponding reactive coordinates not accounted for by TD-DFT methods.

The outer- and inner-valence photoelectron spectra (vertical ionization energies and spectral intensities) of NABs were computed using the ADC(3) scheme [23, 110], i.e., within the one-hole (h) and the two-hole one particle (2h–1p) configurations through third- and first-order, respectively, of the many-body perturbation theory. This technique allows the vertical ionization energies of electronic states to be correctly accounted for when the one-electron picture of ionization is valid [111]. Within this scheme and compared to configuration interaction (CI) treatments having equal accuracy, the ADC(3) method is a less expensive, more compact, and size-consistent method [112–114]. The simulated photoelectron spectra (both energy positions and relative intensities of the bands) issued from this treatment compare quite well with the measured spectra. This permits a correct interpretation for the structures occurring in the inner-valence region of the photoelectron spectrum of NABs [23].

In the last decade, Krylov and coworkers [42, 43] used EOM-IP-CCSD [115–119] and IP-CISD [120] to solve the problematic open-shell states in ionized NABs. These treatments require a "well-behaved" closed-shell neutral wave function. IP-CISD uses uncorrelated Hartree–Fock determinant as a reference, whereas EOM-IP-CCSD uses a correlated CCSD reference. EOM-IP-CCSD is of course more accurate than IP-CISD. These techniques have the advantage of being size-intensive and spin-pure. Through this treatment, several target states and interstate properties are derived. All are used to deduce the ionization energies and the ionization-induced structural changes, and to simulate the photoelectron spectra of NABs [42, 43].

4 Key Results

As mentioned in the introduction, the complexity of the optical spectra increases gradually when going from analogues to the natural NABs. That is why we start out with the presentation of key results for NAB analogues. The natural NABs are presented thereafter, by order of increasing complexity in the spectra.

4.1 NAB Analogues

In recent years, the investigation of ionized NAB analogues has attracted a lot of interest associated with understanding the effects of radiation damage of NABs after their interaction with ionizing radiation, atomic ion beams, and slow or energetic electrons. Here three examples will be treated (3-hydroxyisoquinoline, 2-pyridone/2-hydroxypyridine, and δ-valerolactam). We will show that the complexity of the spectra is related to their electronic structure, to the electronic states' mutual interaction, and to the possible contribution of several tautomers. This complexity increases gradually from 3-hydroxyisoquinoline, to 2-pyridone/ 2-hydroxypyridine, then to δ-valerolactam. The electronic structure of δ-valerolactam resembles those of adenine and of cytosine.

4.1.1 3-Hydroxyisoquinoline

3-Hydroxyisoquinoline (3-HQ) is a NAB analogue. It is considered to be a prototype for the lactam-lactim tautomerism of nitrogen-containing heteroaromatic systems and for studying the effect of electron delocalization on the aromatic ring as well as the electronic structure of NABs. There are a few experimental and theoretical studies on 3-hydroxyisoquinoline treating mainly the mechanisms of tautomerization in the ground and first excited states of this molecule [121–123]. The photoionization of 3-HQ was recently studied for the first time [98].

Scheme 2 displays the PBE0/6-311 + G(d,p) optimized equilibrium structures of neutral and charged forms of 3-HQ (lactim), and of its tautomer (lactam) as computed recently by Pan et al. [98]. The neutral lactim form is more stable than the lactam isomer, in good agreement with the QCISD/cc-pVDZ and QCISD(T)/ cc-pVDZ results based on geometries at the B3LYP/cc-pVDZ level by Gerega et al. [123]. In contrast, the lactam$^+$ is favored with respect to the lactim$^+$. These tautomers are separated by transition states (TS and TS$^+$) where potential barriers for an intramolecular isomerization of more than 1 eV are computed. This is in line with the unique observation, in the experimental IR spectra, of the lactim form trapped in Ar matrices by Gerega et al. [123]. Therefore, jet cooled 3-hydroxyisoquinoline molecular beams are dominated by the lactim
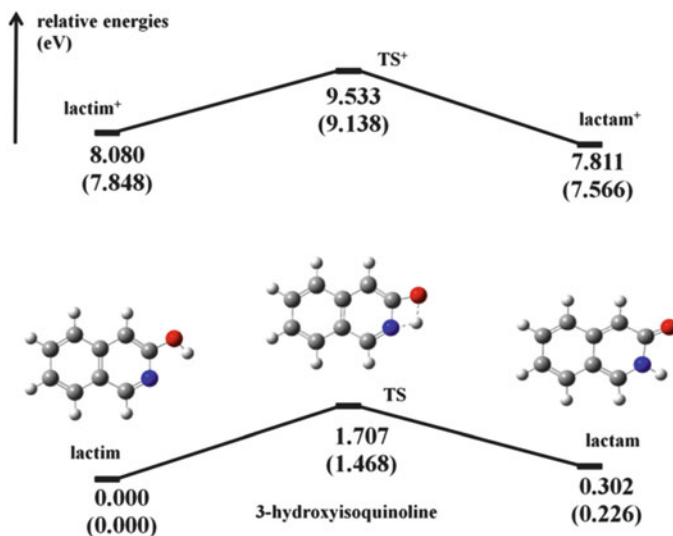
Scheme 2 Structures of the lactim and lactam forms of neutral and cationic 3-hydroxyisoquinoline (lactim 3-HQ). We also give their energetic diagram computed at the (R) CCSD(T)-F12 level of theory including core-valence and scalar relativistic corrections using the equilibrium structure optimized at PBE0/6-311 + G(d,p) level. The relative energies obtained at PBE0 level are shown in parentheses. With permission of [98] Copyright (2013) American Chemical Society

(enol analogue) form unlike the case of 2-pyridone where both tautomers are present and contribute to the photoionization spectra (see below).

Figure 2 displays results obtained from a recent SPI study of gas phase 3-hydroxyisoquinoline measured with VUV light delivered by the SOLEIL synchrotron. The VUV radiation is coupled to the velocity map imaging electron/ion coincidence spectrometer DELICIOUS II as described in detail in [124]. The upper panel of this figure shows the full scale 2D spectrum of 3-hydroxyisoquinoline in the 7.4–9.8 eV photon energy range. The spectrum reveals that the photoionization is found to occur mainly via a direct process near the ionization threshold of 3-hydroxyisoquinoline. The middle panel of Fig. 2 presents the SPES of this lactim. This spectrum has been assigned with the help of theoretical calculations at the MRCI(+Q)/CASSCF/aug-cc-pVDZ level for the electronic states patterns and at the PBE0/6-311 + G(d,p) level for the harmonic and anharmonic wavenumbers of the lactim and lactam forms of 3-hydroxyisoquinoline and their cations.

As can be seen in Fig. 2, there is no electron signal around 7.5 eV where one may expect the formation of the lactam cationic form according to our theoretical value of 7.509 eV, predicted at the (R)CCSD(T)-F12/cc-pVTZ-F12 level and where core valence and scalar relativistic factors are also taken into consideration. Hence, there is no evidence for the formation of a lactam[+] isomer upon ionization of the lactim isomer, most likely because of the relatively high tautomerism barriers in both the neutral and ionic species (cf. Scheme 2). With the help of the explicitly correlated
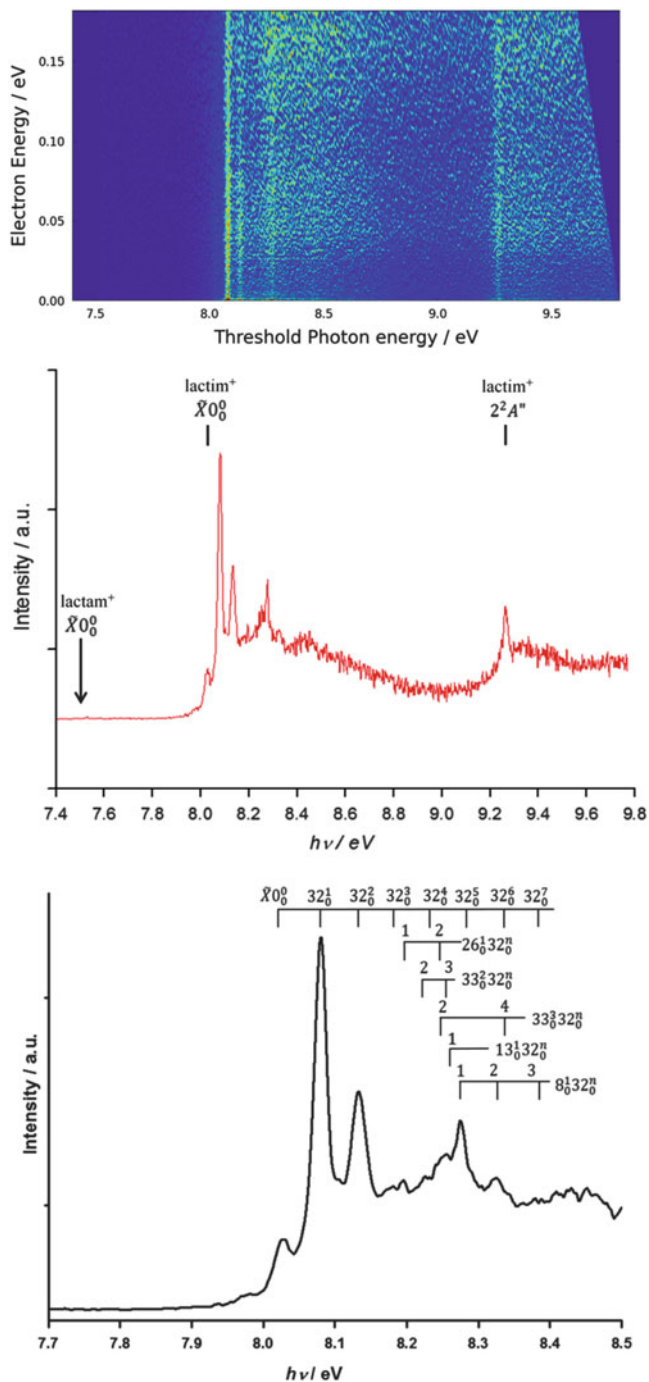
Fig. 2 *Upper panel*: Full scale 2D spectrum of 3-hydroxyisoquinoline. This spectrum gives the photoelectron kinetic energies vs the photon energy. *Middle panel*: Slow photoelectron spectrum (SPES) (*red line*) deduced from the 2D spectrum. *Lower panel*: Blow-up of the SPES spectrum in

Table 1 Dominant electron configurations and MRCI and MRCI + Q vertical excitation energies (in eV) of the ground and excited states of doublet lactim$^+$ (enol) of 3-hydroxyisoquinoline. These energies are given with respect to the $\widetilde{X}^1A'$ minimum of neutral 3-hydroxyisoquinoline lactim

State	Electron configuration	MRCI	MRCI + Q
$\widetilde{X}^2A''$	$0.92 \times \{(30a'')^2(31a')^2(32a')^2(4a'')^2(5a'')^2(6a'')^1\}$	7.40	7.55
$2^2A''$	$0.88 \times \{(30a')^2(31a')^2(32a')^2(4a'')^2(5a'')^1(6a'')^2\}$	9.30	9.30
$1^2A'$	$0.90 \times \{(30a')^2(31a')^2(32a')^1(4a'')^2(5a'')^2(6a'')^2\}$	11.04	10.26
$3^2A''$	$0.80 \times \{(30a')^2(31a')^2(32a')^2(4a'')^1(5a'')^2(6a'')^2\}$	10.84	10.84
$4^2A''$	$0.85 \times \{(30a')^2(31a')^2(32a')^2(4a'')^2(5a'')^2(7a'')^1\}$	11.95	11.69
$2^2A'$	$0.74 \times \{(30a')^2(31a')^2(32a')^1(4a'')^2(5a'')^2(6a'')^1(7a'')^1\}$	14.11	13.30
$5^2A''$	$0.59 \times \{(30a')^2(31a')^2(32a')^2(4a'')^2(5a'')^2(8a'')^1\}$ $+0.57 \times \{(30a')^2(31a')^2(32a')^2(4a'')^2(5a'')^1(6a'')^1(7a'')^1\}$	14.04	13.43
$3^2A'$	$0.90 \times \{(30a')^2(31a')^2(32a')^2(33a')^1(4a'')^2(5a'')^2\}$	14.35	13.74
$4^2A'$	$0.90 \times \{(30a')^2(31a')^1(32a')^2(4a'')^2(5a'')^2(6a'')^2\}$	14.86	14.33
$5^2A'$	$0.91 \times \{(30a')^1(31a')^2(32a')^2(4a'')^1(5a'')^2(6a'')^2\}$	14.96	15.01

This table is adapted from [98]

computations results, the first dominant peak (at $h\nu = 8.028$ eV) is tentatively assigned as the band origin for the ionization transition of lactim. The corresponding theoretical IE (of 8.080 eV) coincides, within the theoretical and experimental error bars, with the experimental IE(lactim) = 8.028 eV value deduced from this SPES spectrum (cf. Fig. 2). In contrast, the theoretical DFT IE (of 7.848 eV) is off by ~0.2 eV as expected for such a level of theory. Moreover, a rich vibrational structure is observed that corresponds to vibrational transitions (single mode or combinations) populating the cationic lactim$^+$ ground state $\widetilde{X}$ vibrational levels. A key feature of the assignment is the strong transition at 8.08 eV. This transition is assigned to a vibrational mode (ν_{32}^+) which corresponds mainly to the angular deformation (in-plane) involving the C10–C14–O17 and N16–C14–O17 angles, which represent the major geometrical differences between 3-hydroxyisoquinoline lactim and lactim$^+$ forms (cf. lower panel of Fig. 2 which illustrates tentative assignments of observed vibrational bands in the 7.7 to 8.5 eV region).

In addition, several weaker and complex bands are observed in the SPES spectrum above 9 eV. They correspond to the population of vibrational levels of the $\widetilde{A}$ electronically excited state of the cation. The $\widetilde{A}$ state is predicted to lie at these energies (cf. Table 1). At higher energies, a high density of electronic states is predicted (cf. Table 1) that will favor their mutual interaction by vibronic coupling. Vibronic coupling and predissociation will participate to congestion of the bands in this energy region.

Fig. 2 (continued) the 7.7–8.5 eV region where the comb lines correspond to the tentative assignments. Reprinted with permission from Pan et al. [98]. Copyright (2013) American Chemical Society

Scheme 3 2-Pyridone (2-PY$^+$) cation and its tautomer 2-hydroxypyridine (2-HP$^+$)


2-PY$^+$ **2-HP$^+$**
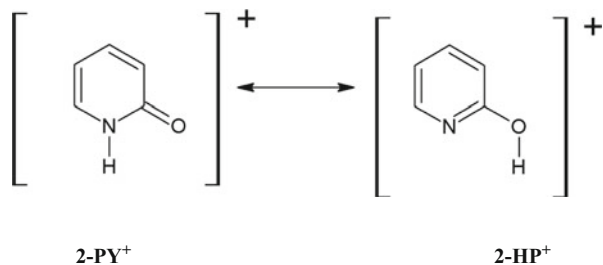
4.1.2 2-Pyridone

2-Pyridone (lactam, 2-PY), its tautomer 2-hydroxypyridine (lactim, 2-HP) (cf. Scheme 3), and their dimers together represent a model system to study NABs, isolated or paired, as well as the hydrogen bonding in their complexes. The neutral species were widely studied experimentally and theoretically as detailed in [9, 94]. Mainly, the work published in these references accurately characterized the equilibrium structure of both tautomers, their relative energies, and their electronic excited states. In contrast, only a few studies considered their cations.

In 2002, Trikoupis et al. [125] performed combined B3LYP/CBSB7 computations and mass spectrometric experiments on 2-HP$^+$. They showed that the fragmentation pathways of the cationic species are very complex. Indeed, 2-HP$^+$ undergoes decarbonylation to yield 3-H pyrrole ions and CO (pathway (b) in Scheme 4) after ring-opening. Alternatively, the reaction may proceed through the most stable form, 2-PY$^+$, after 1,3-H transfer through a 28 kcal/mol ketonization barrier (pathway (a) in Scheme 4).

The IEs of 2-PY and of 2-HP were determined by electron impact ionization [126], photoelectron [127], resonance enhanced multiphoton ionization [128], zero kinetic energy (ZEKE) photoelectron, resonantly enhanced two-photon ionization, and mass analyzed threshold ionization (MATI) spectroscopies [129, 130], and more recently by slow photoelectron spectroscopy [9]. For 2-PY, ZEKE spectra provided an IE (2-PY) of 8.4479 ± 0.0006 eV and IE (2-HP) of 8.9384 ± 0.0006 eV [129], which were confirmed later by the SPES study of Poully et al. [9]. Of potential interest, the corresponding spectra (Figs. 3 and 4) present rich structures, which correspond to the population of the vibrational levels of the 2-PY$^+$ cation in the $\widetilde{X}$ ground and $\widetilde{A}$ excited electronic states, as well as of the 2-HP$^+$ cation in the electronic ground state. The SPES spectrum (Fig. 4) displays the assignment of these bands based on the PBE0/6-311 + G(d,p) computation results listed in Table 2. Because of symmetry selection rules, only the a' cationic levels are populated by one photon ionization from the corresponding neutral ground state. These bands are mainly due to excitation of the cationic vibrational modes 18 and 20 together with weaker contributions of bands involving other vibrational modes and even numbers of quanta of the vibrational mode 21 (cf. Table 2). Moreover, the analysis of the SPES spectrum allows the determination of some fundamentals of 2-PY$^+$,

Scheme 4 Schematic representation of the unimolecular processes undertaken by 2-HP$^+$. Energies are in kcal/mol. The energetics of pathways a and b are unknown. With courtesy of [125]
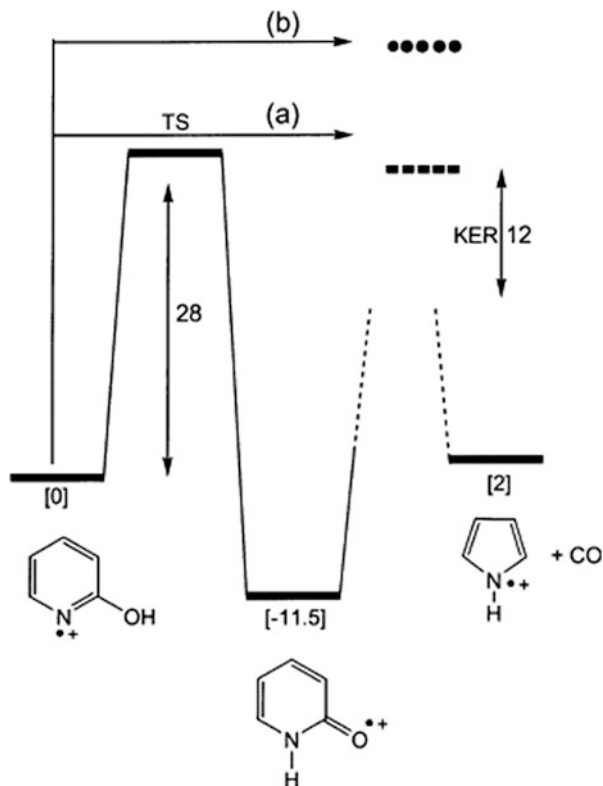
i.e., $\nu_{20}^+ = 521$, $\nu_{18}^+ = 739$, $\nu_{16}^+ = 1005$, $\nu_{13}^+ = 1223$, $\nu_{11}^+ = 1356$, $\nu_{10}^+ \approx \nu_9^+ = 1452$, and $\nu_8^+ \approx \nu_7^+ = 1573$ (all values are in cm^{-1}). The experimental values from ZEKE measurements are very close to those obtained using SPES spectroscopy since deviations between both sets of data are less than 4 cm^{-1}. For instance, the ZEKE ν_{20}^+, ν_{16}^+, ν_{13}^+, ν_{10}^+ / ν_9^+, and ν_8^+ / ν_7^+ fundamentals were measured at 520, 1,010, 1,219, 1,457, and 1,572 (in cm^{-1}), respectively. Generally, the experimental and theoretical values agree quite well, which validates the use of the PBE0/6-311+G(d,p) method for deduction of anharmonic frequencies of such classes of molecules. In addition, the 2D-SPES spectrum reveals that photoionization of 2-PY and of 2-HP molecules occurs mainly via a direct process close to their ionization thresholds, whereas the indirect route (autoionization) may contribute at higher energies.

Finally, the recent theoretical study [96] of the spectroscopy of methyl substituted 2-pyridones, tautomers and ions (denoted as xMe-2-PY$^{0/+1}$ and xMe-2-HP$^{0/+1}$, where x represents the relative position of the methyl group on the ring) and comparison to 2-PY$^{0/+1}$ and to 2-HP$^{0/+1}$ showed that there is a lowering of all vibrational frequencies upon ionization and that the substitution of an H by the methyl group enhances such reduction. Shifts for short wavelengths were computed, with the largest effect being predicted for 6Me-2-HP. The effects are large for the CO stretching mode, whereas the NH stretching mode varies only slightly.
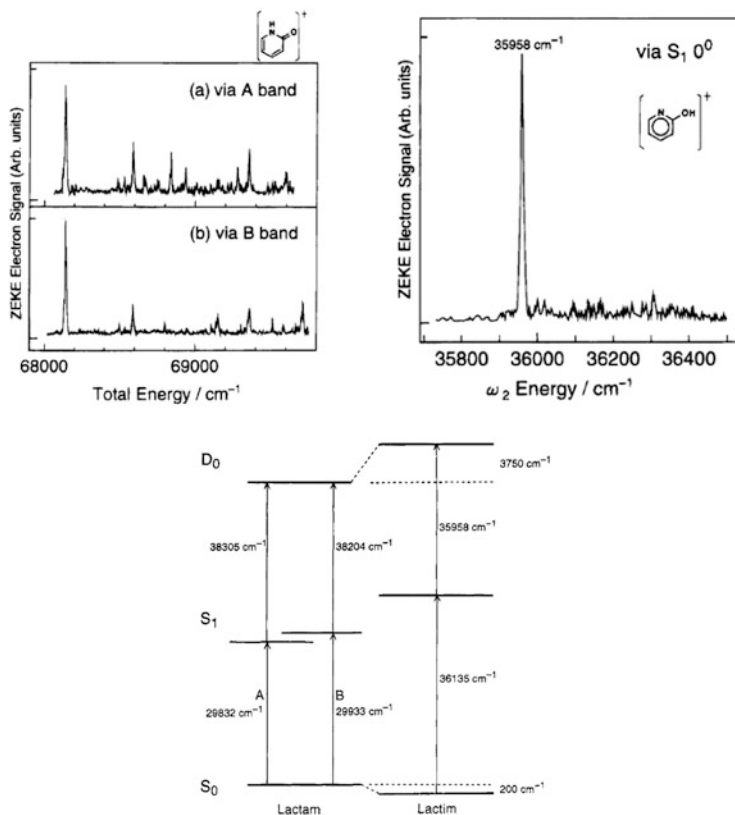
Fig. 3 ZEKE photoelectron spectrum of 2-PY (lactam, *upper left panel*), of 2-HP (lactim) via the S1 neutral state (*upper right panel*), and energy diagram of 2-PY and of 2-HP (*lower panel*). Reprinted with permission from Ozeki et al. [129]. Copyright (1995) American Chemical Society

The computed frequency changes observed for the methyl compounds are large enough to be measurable by means of modern spectroscopic techniques.

The lowering of the frequencies upon ionization or methyl substitution is due to the perturbation of the π electron distribution on the aromatic ring. Indeed, ionization induces a loss of π electrons and the donor electronic effect of methyl leads to "excess" electrons on the ring. Both effects result on deviations from the $4n+2$ electrons rule for perfect aromaticity.

4.1.3 δ-Valerolactam

δ-Valerolactam (piperidin-2-one) is a cyclic lactam (cf. Scheme 5). There are structural similarities between δ-valerolactam (saturated C–C bonds) and 2-pyridone (aromatic six ring cycle). δ-Valerolactam presents a small number of
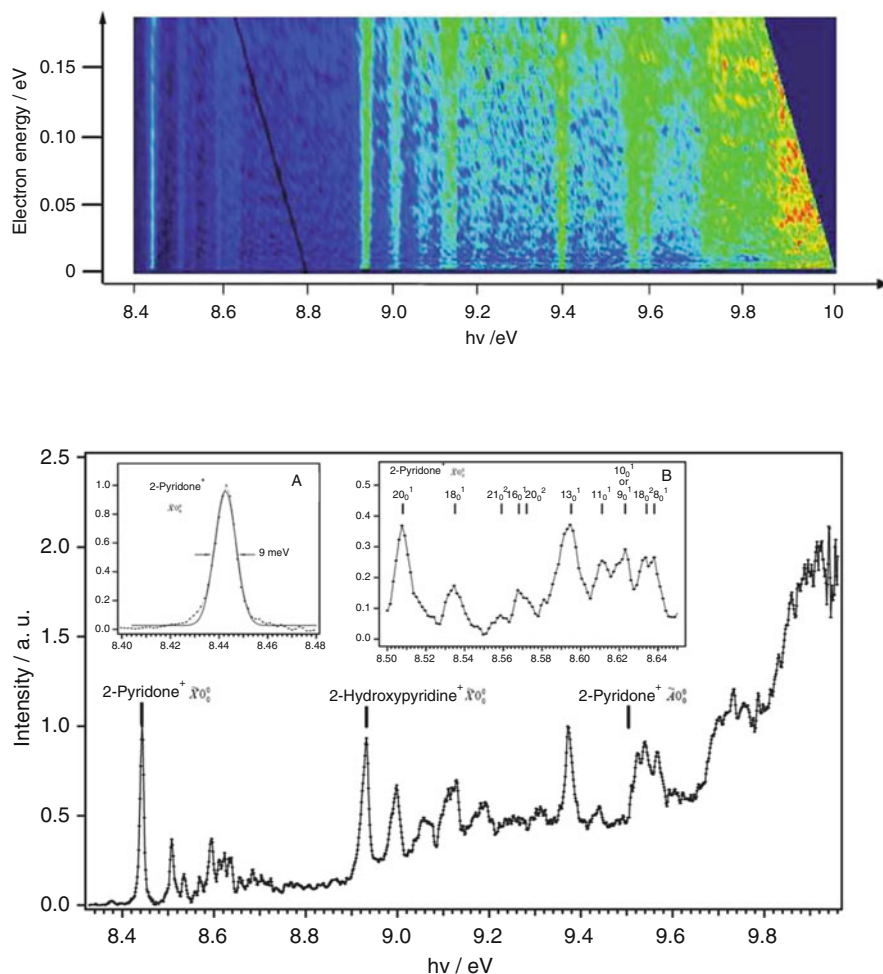
Fig. 4 *Upper panel*: Full scale 2D SPES spectrum of 2-PY and of 2-HP. It gives the photoelectron kinetic energies vs the photon energy. *Lower panel*: Slow photoelectron spectrum (SPES) for electron kinetic energies from 0 to 75 meV. We highlight the experimentally-determined origin transitions for the ground state of 2-PY$^+$ and of 2-HP$^+$. The *insets* correspond to a zoom of this spectrum in the region 8.40–8.65 eV, where the vertical lines reproduce the assignments of the bands. Reproduced from [9] by permission of the PCCP Owner Societies

hydrogen bonding donor-acceptor sites. It represents an even simpler model for studying the pairing (hydrogen bonding) between NAB pairs since only the amide form predominates under laboratory conditions, whereas 2-pyridone possesses two tautomers (lactam and lactim forms). Several structural and spectroscopic studies were performed on the neutral δ-valerolactam molecule. They are reviewed in [95]. For the cation, Potapov et al. [131] and Treschanke and Rademacher [132, 133] determined the IEs of δ-valerolactam, at IE $= 9.15 \pm 0.02$ and 9.30 eV,

Table 2 PBE0/6-311 + G (d,p) fundamental harmonic and anharmonic frequencies (in cm^{-1}) of 2-PY$^+$ and 2-HP$^+$ cations [Hammoutène et al. Private communication]. For 2-PY$^+$, modes 1–21 are of a$'$ symmetry and modes 22–30 are of a symmetry. For 2-HP$^+$, all modes are of a symmetry

Mode	2-PY$^+$		2-HP$^+$	
	Harmonic	Anharmonic	Harmonic	Anharmonic
1	3,547.4	3,385.4	3,782.4	3,579.7
2	3,243.7	3,123.8	3,236.2	3,108.6
3	3,237.6	3,113.6	3,225.6	3,098.9
4	3,224.3	3,085.0	3,204.2	3,076.0
5	3,220.3	3,091.9	3,196.6	3,062.5
6	1,637.5	1,596.8	1,631.7	1,589.4
7	1,595.6	1,568.3	1,571.1	1,540.1
8	1,581.6	1,561.5	1,500.6	1,466.8
9	1,491.1	1,458.4	1,474.6	1,450.1
10	1,484.2	1,454.8	1,445.8	1,412.7
11	1,388.5	1,355.9	1,396.4	1,365.7
12	1,270.0	1,243.2	1,359.7	1,329.0
13	1,241.8	1,212.3	1,178.3	1,148.5
14	1,180.8	1,165.1	1,158.9	1,120.7
15	1,098.4	1,081.3	1,119.4	1,096.0
16	1,037.0	1,018.9	1,011.8	1,015.0
17	994.0	983.3	1,009.9	992.6
18	789.1	770.3	989.1	981.4
19	604.4	596.2	985.7	965.5
20	538.3	531.9	864.4	845.1
21	452.4	448.6	827.0	829.6
22	1,022.5	1,015.6	776.6	748.7
23	1,011.1	1,016.9	675.8	656.9
24	919.4	913.6	602.9	575.2
25	813.9	810.6	601.2	588.3
26	766.9	762.1	552.0	533.5
27	670.9	670.1	448.0	436.5
28	450.1	451.7	431.6	427.3
29	350.1	348.4	353.6	352.1
30	177.8	175.6	124.1	124.7

respectively by means of HeI photoelectron spectroscopy. Their spectra are composed of well-resolved bands extending over ~1 eV each which were attributed to ionization from π_N, n_O for the first two bands and to the inner valence shell ionization for the higher ones. Recently, Mahjoub et al. [95] studied the single photon ionization of gas phase δ-valerolactam and the state-to-state fragmentation of [δ-valerolactam]$^+$ by means of VUV synchrotron radiation coupled to a velocity map imaging electron/ion coincidence spectrometer [97]. These authors have also performed extensive state-of-the-art computations on equilibrium geometries, electronic state patterns, and evolutions, harmonic, and anharmonic frequencies of neutral and positively charged δ-valerolactam, and for over 170 possible dissociation channel products. The equilibrium structure computations were done at the PBE0/aug-cc-pVDZ and the MP2/aug-cc-pVTZ levels of theory. The mapping of
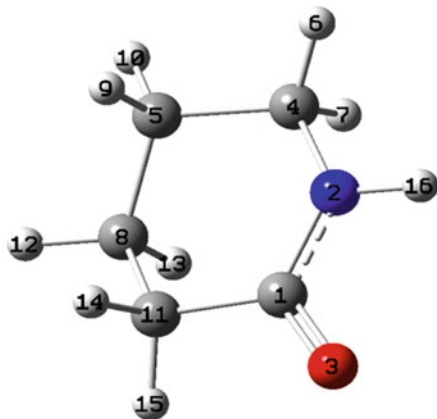
the electronic states of the cation was done at MRCI + Q/CASSCF/aug-cc-pVDZ level of theory.

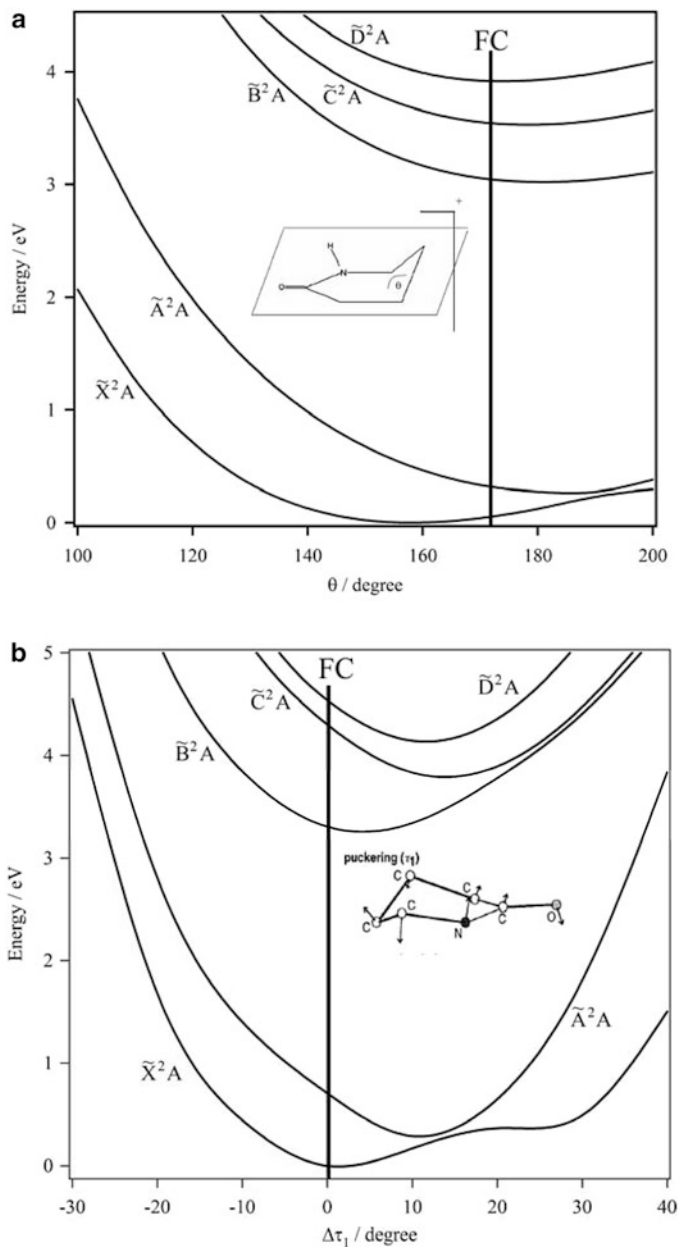We display in Fig. 5 the CASSCF/aug-cc-pVDZ one-dimensional evolutions of the potential energy surfaces of the lowest doublet electronic states of [δ-valerolactam]$^+$ along the planarization angle θ and along the normal coordinate relative to the out-of-plane torsion mode 41 [95]. This figure reveals that the ground electronic state $\widetilde{X}^2A$ and the first excited state $\widetilde{A}^2A$ become close to each other for θ ~ 190° and Δτ ~ 14°. An avoided crossing is visible at these nuclear configurations, i.e., close to the equilibrium molecular structure of the $\widetilde{A}^2A$ state. Consequently, both electronic states are coupled vibronically and their electronic wave functions are strongly mixed, resulting in complex and non-conventional rovibronic spectra for the $\widetilde{X}^2A$ and $\widetilde{A}^2A$ states in the vicinity of this avoided crossing (not sufficiently resolved in the SPES experimental study). Theoretically, accurate derivation of the spectrum of these states needs further development, where the potential energy surfaces of both states should be mapped in full dimensionality and a variational treatment of the nuclear motions is needed.

Figure 6 (upper panel) displays the full scale 2D spectrum of jet cooled δ-valerolactam providing the photo-electron kinetic energies vs the photon energy. This spectrum shows that photoionization of this molecule takes place mainly via a direct process close to the ionization thresholds whereas the indirect route (autoionization) contributes at higher energies. The SPES for electron kinetic energies from 0 to 57 meV as deduced from the 2D spectrum is also given (Fig. 6, middle panel). The vertical bars correspond to the theoretically-determined electronic state origin transitions. At the MRCI + Q/CASSCF/aug-cc-pVDZ level of theory, the $\widetilde{A}^2A, \widetilde{B}^2A, \widetilde{C}^2A,$ and $\widetilde{D}^2A$ states are computed to lie at 0.52, 2.90, 3.22, and 3.55 eV with respect to the [δ-valerolactam]$^+$ $\widetilde{X}^2A$ energy at equilibrium. These energies fit quite well with the origin bands of this SPES spectrum and compare quite well to those deduced from the HeI photoelectron spectrum of Treschanke and Rademacher [133] (at 0.5, 2.1, 2.8, and 3.0 eV, with respect to the ground state

Fig. 5 (**a**) CASSCF/aug-cc-pVDZ one-dimensional cuts of the potential energy surfaces of the lowest doublet electronic states of δ-valerolactam$^+$ along the planarization coordinate, θ. The remaining internal coordinates are kept fixed at their equilibrium values in δ-valerolactam$^+$ $\widetilde{X}$. (**b**) CASSCF/aug-cc-pVDZ one-dimensional cuts of the potential energy surfaces of the lowest doublet electronic states of δ-valerolactam$^+$ along the normal coordinate, $\Delta\tau_1$ (mode 41). These curves are given in energy with respect to the energy of δ-valerolactam$^+$ $\widetilde{X}$ at equilibrium. The *solid*

origin band of the cation). The synthetic spectrum in Fig. 6 illustrates the good agreement between experiment and theory.

The narrow bands at the left side of the slow photoelectron spectrum correspond to transitions populating vibrational levels of the cation $\widetilde{X}$ state. Moreover, several weaker and complex bands are observed, corresponding to population of vibrational levels (single or combination modes) of the electronically excited states of the cation arising from their mutual vibronic interactions. This is shown in the lower panel of Fig. 6 as an inset which corresponds to an enlargement of the SPES spectrum in the vicinity of the cationic ground state. The tentative assignment of the observed bands (vertical lines) is achieved with the help of the theoretical results [95].

After its formation, the [δ-valerolactam]$^+$ ion is subject to isolated state intramolecular unimolecular fragmentation processes. The time-of-flight mass spectra at different photon energies from 9 to 12 eV are displayed in Fig. 7. Various fragments of [δ-valerolactam]$^+$ parent cation are observed, corresponding to m/z 30, 43, 56, 58, 70, 71, 82, and 98. Tentative identifications of the related fragmentation pathways based on ab initio computational results are given in Table 3. Generally, close analysis of the products shows that isolated state unimolecular decomposition of this NAB analogue leads mostly to nitriles and small heterocycles. These kinds of molecules can be qualified as "prebiotic" since they can themselves be precursors of the building blocks of life (amino acids and NABs). The reversed reactions of NAB dissociation may thus be of importance for the synthesis of these species in a prebiotic environment. Further experimental investigations in the laboratory are needed for confirmation.

4.2 NABs Occurring in Biological DNA and RNA

4.2.1 Thymine

The experimental adiabatic ionization energy of thymine (T) is found at AIE $= 8.82 \pm 0.03$ eV by Jochims et al. [37]. PE spectra of thymine have been measured by several groups [15–17, 20, 23]. According to ab initio calculations, thymine, unlike cytosine, for example (see below), has no low-lying tautomers [134]. The most stable form is a diketo isomer followed by an enol form at ~45 kJ/mol higher in energy. Eleven other tautomers are identified, with energies up to 130 kJ/mol above the most stable one. The room temperature PE spectrum is therefore not complicated by the contribution of several tautomers prior to
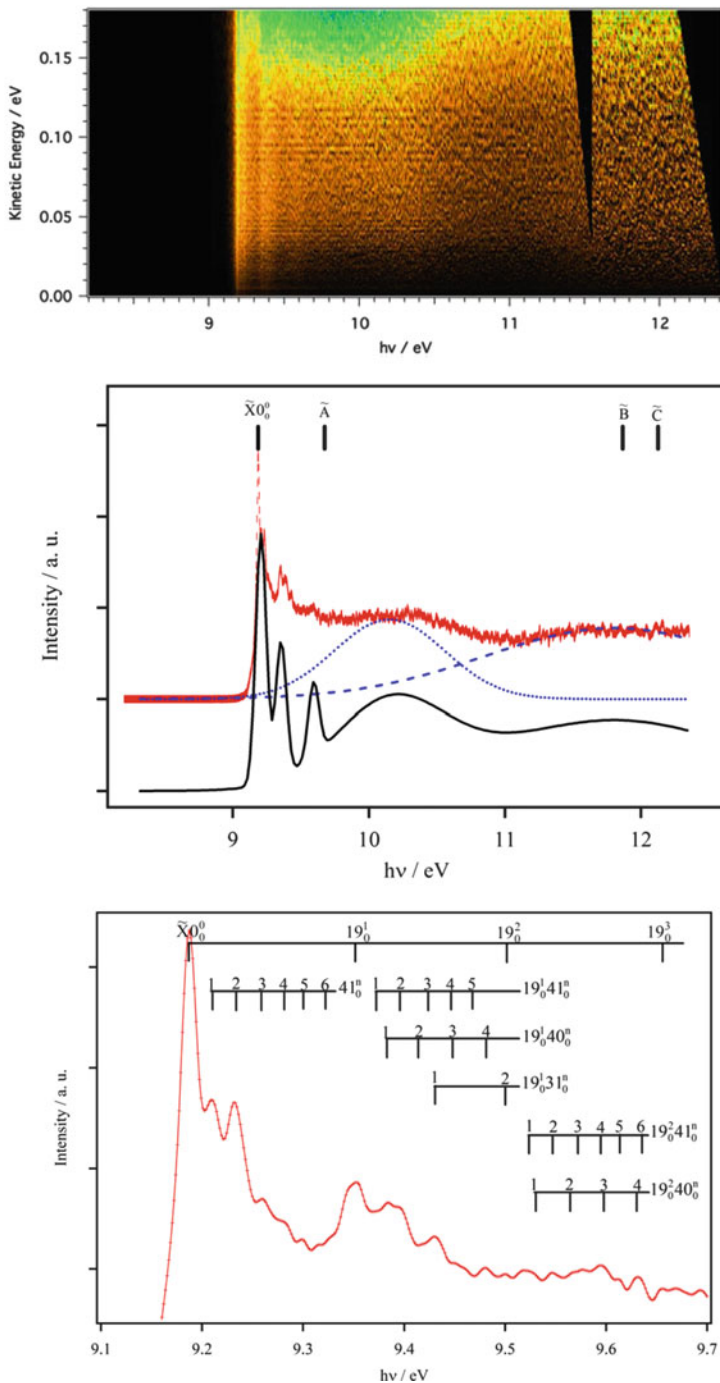
Fig. 6 *Upper panel*: Full scale 2D spectrum of δ-valerolactam providing the photo-electron kinetic energies vs the photon energy. *Middle panel*: Slow photoelectron spectrum (SPES) (*red line*) for electron kinetic energies from 0 to 57 meV as deduced from the 2D spectrum.
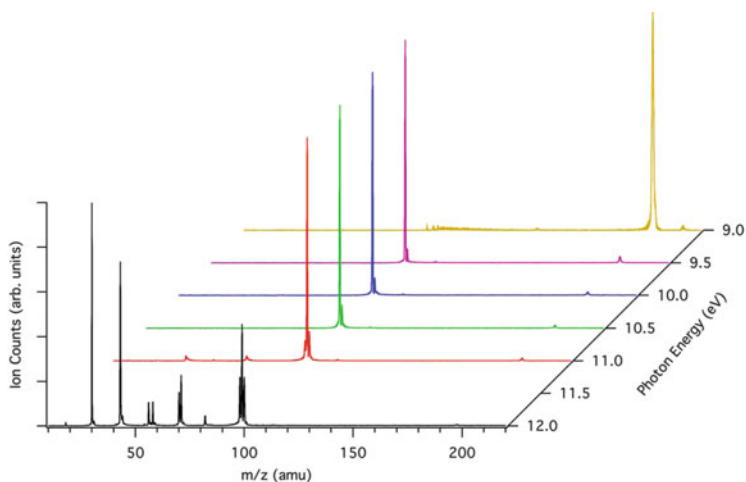
Fig. 7 Time-of-flight (TOF) spectra of δ-valerolactam recorded at six fixed photon energies from 9.0 to 12.0 eV. Reprinted with permission from Mahjoub et al. [97]. Copyright (2012) American Chemical Society
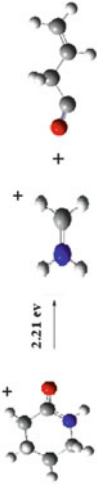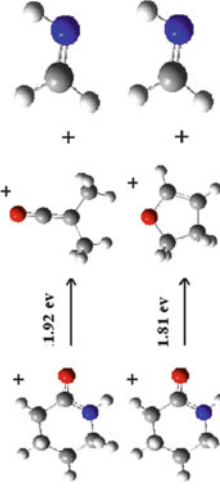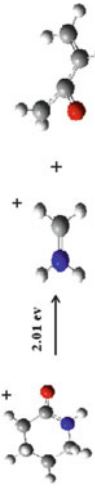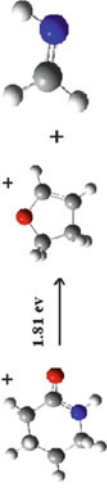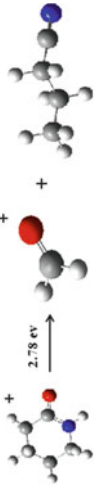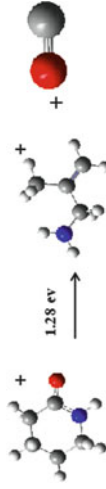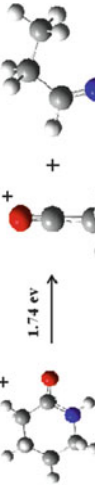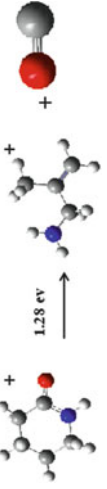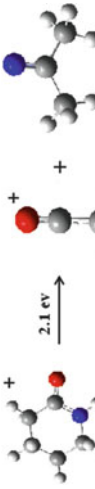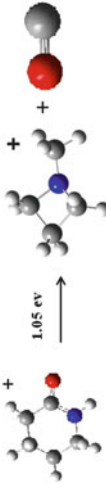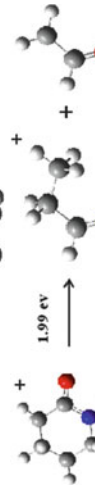
ionization. However, rotation of the methyl group gives rise to two possible conformers, *cis* and *trans*. Trofimov et al. [23] have calculated the binding energies (BEs) and spectral band intensities in the 8.82 to 17.35 eV energy range using OVGF and ADC methods. Satisfactory agreement with their own and previous experimental spectra is achieved even though some of the electronic PE bands overlap and proper assignment, especially above 14 eV, becomes difficult. In their work, angle-dependent PE measurements helped to distinguish σ from π orbitals in the assignment. To give an extract from this excellent work, the lowest molecular orbitals of T have the following character and BE: $6a''(\pi_6)$, BE = 8.85 eV (OVGF, 6-311++G** basis set); $5a''$ (π_5), BE = 10.46 eV, $18a'$ (σ_{LP-O}), BE = 10.46 eV; $17a'$ (σ_{LP-O}), BE = 11.36 eV; $4a''(\pi_4)$, BE = 12.52 eV. The following, more uncertain assignments can be found in [23].
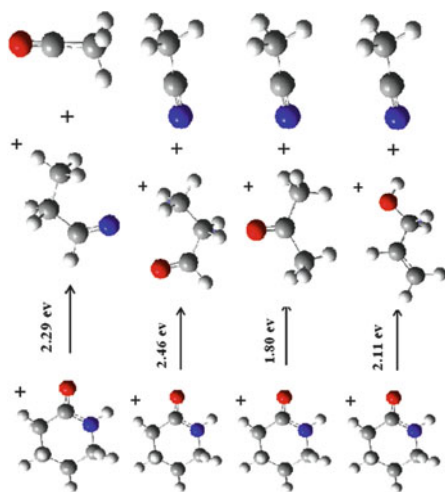
Very shortly after this work, a Mass-Analyzed Threshold Ionization (MATI) spectrum was measured with high resolution (~0.1 meV). This spectrum (Fig. 8) corresponds to the photoionization of jet-cooled T close to the ionization threshold region, between its IE and IE + 1,800 cm^{-1} (IE + 0.22 eV) [135]. It presents a rich structure that was attributed to the population of the lowest vibrational levels of the

---

Fig. 6 (continued) We highlight the theoretically determined origin transitions with *vertical bars*. The synthetic spectrum (*black line*) is obtained after a rough adjustment of the experimental spectra assuming few Gaussian profiles: the narrow bands at the left side are for the ground state and the larger ones are for the two contributing autoionizing states (the *dotted* and *dashed blue lines*). *Lower panel*: SPES spectrum of delta-valerolactam$^+$ in the vicinity of the cationic ground state and its tentative assignment (*vertical lines*) by the help of the theoretical results [95]. Copyright © Wiley-VCH Verlag GmbH & Co. KGaA, Weinheim

Table 3 Experimental linear extrapolated appearance energies (AE$_{exp}$, eV) for all the masses observed in the photodissociation of δ-valerolactam, along with their calculated fragmentation pathways

Mass (amu)	AE$_{exp}$	Calculated channel	Mass (amu)	AE$_{exp}$	Calculated channel
30	2.19	2.21 eV	70	1.22 1.92	1.92 eV / 1.81 eV
43	1.42 1.96	2.01 eV / 2.78 eV	71	1.22 1.92	1.28 eV / 1.05 eV
56	2.00	1.74 eV / 2.1 eV / 1.99 eV	82	1.99	Several possibilities below 1.34 eV[a]
			98	1.07 1.85	δ-Valerolactam$^+$ H loss (1.49 eV)

58

1.95

2.29 ev

2.46 ev

1.80 ev
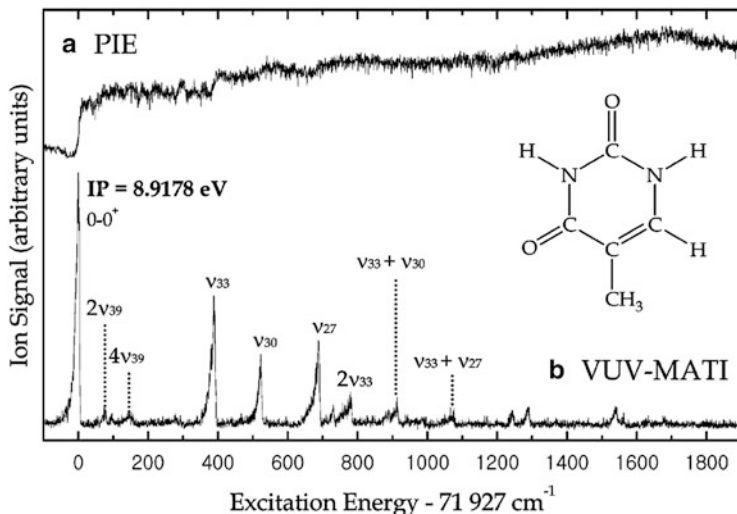
2.11 ev

[a]See [97] for more details

Fig. 8 (**a**) Photoionization efficiency (PIE) and (**b**) VUV-MATI spectrum of thymine. Spectrum (**b**), recorded by nanosecond VUV laser spectroscopy (resolution ~0.8 cm^{-1}), can be regarded as a most highly resolved VUV spectrum in the IE + 1,800 cm^{-1} region for a biological NAB. For the normal mode analysis of the S_0–D_0 transition of thymine please refer to [135]. Reprinted with permission from Choi et al. [135]. Copyright (2005) American Chemical Society

T$^+$ cation. The first normal-mode analysis of T$^+$ for the observed vibrational structure is also presented in the work of Choi et al. [135]. It is shown that the observed bands correspond to the population of the low frequency modes ν_{27}, ν_{30}, ν_{33}, and ν_{39} of T$^+$. In addition, this spectrum is dominated by the 0–0 transition and the adiabatic IE is thus measured accurately to be AIE = 8.9178 ± 0.001 eV. The discrepancy with the value found by Jochims et al. [37], of the order of 0.1 eV, is most reasonably explained by the initial thermal energy content of the thymine neutrals produced by the source used in [37].

Later on, Bravaya et al. [43] presented a complete theoretical vibrational analysis of the S_0–D_0 transition between its origin and 9.7 eV. These authors used the high resolution MATI spectrum of Choi et al. [135] to test the quality of their calculations. In terms of accuracy in energy position, there is excellent agreement, since the theoretical AIE is computed at 8.89 eV, which differs by only ~0.02 eV from the AIE of [135]. The positions and relative intensities of the experimental vibrational bands are also nicely reproduced by the (blue-shifted) theoretical spectrum of [43] in the region between the AIE and AIE + 0.1 eV approximately (see Fig. 10 in [43]). This validates the approximation they used to compute the Franck–Condon Factors (FCF) for interpretation and prediction of experimental PESs. The authors of [43] then continue to calculate the full vibrational progression of the S_0–D_0 transition of the PES (up to AIE + 1 eV). However, in this spectral region there are considerable deviations to the experimental PES of [23]. They are explained by possible mixing with the S_0–D_1 progression, which makes sense, since
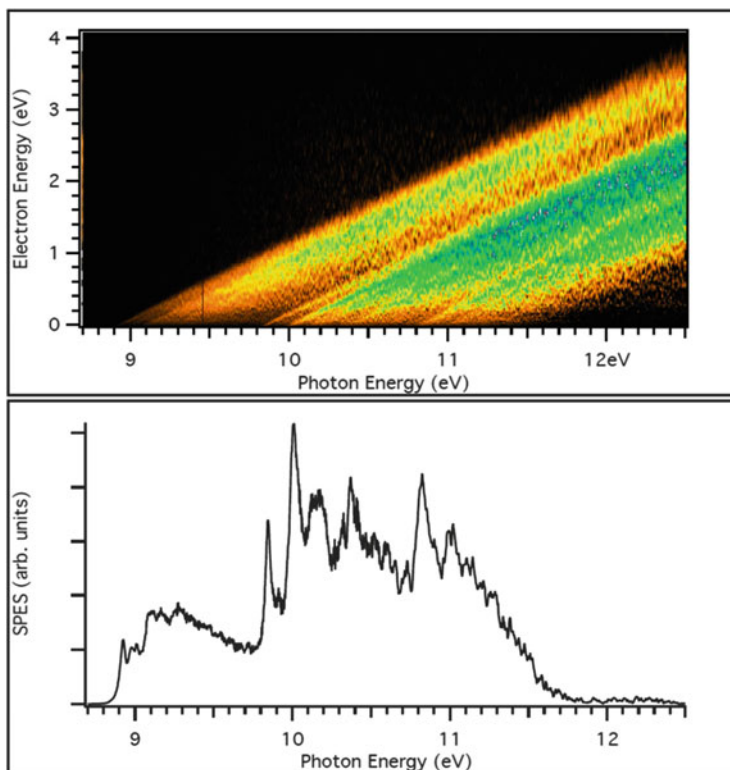
Fig. 9 *Upper panel*: PES matrix corresponding to the thymine parent mass, obtained with oven vaporization. The energy step is 2.5 meV. *Lower panel*: SPES derived from the PES matrix by considering photoelectrons having kinetic energies less or equal 200 meV [136]

this transition is much more intense and its precise origin is not well known. Vertical ionization energies have also been calculated for the six lowest ionized electronic states of thymine by different methods. The order is found to be in agreement with the results of Trofimov et al. [23]. We note that experimental PES band positions are satisfactorily reproduced by the differentiated PIE spectrum (dPIE/dE) also presented in [43]; however, the relative spectral intensities of the experimental PES bands from [23] are not reproduced by the dPIE/dE curve.

Very recently, Majdi et al. [136] have recorded a thymine SPES spectrum at the SOLEIL synchrotron, under similar conditions to those depicted in [11] for adenine and cytosine. This spectrum is shown in Fig. 9. Strikingly, the SPES spectrum (Fig. 9, lower panel) presents rich and well-resolved structures that correspond to the electronic and vibrational structures of thymine$^+$ cation. This work extends the experimental spectrum of Choi et al. [135]. The full analysis of these bands is under investigation. The experimental work of Majdi et al. [136] reveals that the experimental capabilities at the DESIRS beamline of the SOLEIL synchrotron are powerful enough to get insight into the NABs cationic structure. It confirms our
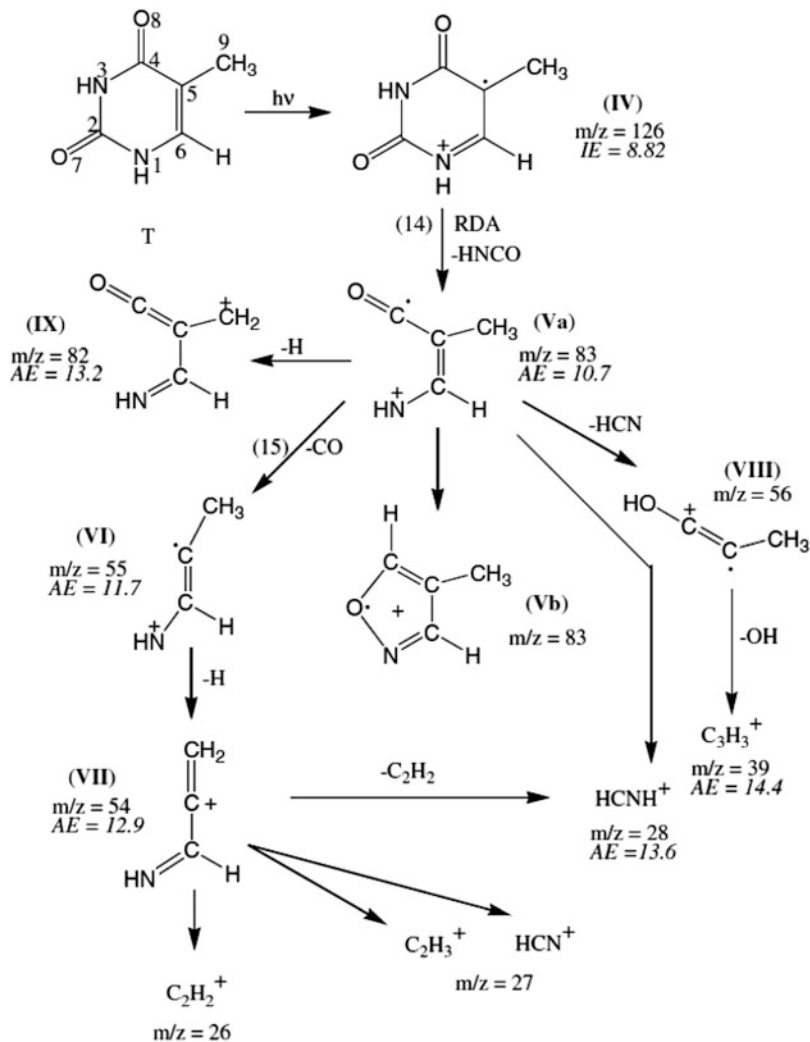
Fig. 10 Principal fragmentation decay routes of the thymine radical cation. Measured appearance energy (AE) is given for each fragment (in eV). *Roman numerals* correspond to species discussed in [37]. Reprinted from Jochims et al. [37]. Copyright (2005), with permission from Elsevier

analysis for adenine and cytosine [11] where the congestion of the spectra resides in fact in the intrinsic complex electronic, tautomeric, and vibronic structure of adenine and cytosine (see also below).

The dissociative ionization of T was studied in detail by Jochims et al. [37]. The three main dissociation pathways, shown in Fig. 10, are as follows. (1) The loss of isocyanic acid (HNCO) by retro-Diels–Alder reaction from the thymine parent cation, to form the m/z 83 residual fragment with an AE of 10.7 ± 0.05 eV. The loss

of HNCO involves rupture of two bonds, N3–C4 and C2–N1. The latter bond is shown to be weaker in the cation as compared to the neutral thymine [69]. (2) The subsequent loss of CO together with a fragment of m/z 55 and AE $= 11.7 \pm 0.1$ eV. As was shown above, the loss of a CO is the lowest fragmentation channel of the 2-PY$^+$ and 2HP$^+$ analogues. (3) Another intense ion is seen at m/z 28 (AE $= 13.6 \pm 0.1$ eV). It is assigned to the HCNH$^+$ ion (an ion observed in the interstellar medium). Other ions, with lower intensity are also detected. Possible assignments of the chemical structures of observed ions and corresponding neutral fragments, as well as formation pathways, are discussed in detail in [37].

4.2.2 Uracil

This RNA NAB has been less studied in the past decade than the other biological NABs. Early PE spectra are reported in [15–17, 20, 21]. As one can expect from the similarity of the chemical structure, the PE spectrum of uracil resembles closely the PE spectrum of thymine (see, for example, [20]). According to the analysis presented in [21], the four lowest lying molecular orbitals are of π_1, n_1, π_2, and n_2 character, respectively. They lie very close in energy (VIE (exptl.) $= 9.53$, 10.23, 10.57, and 10.99 in eV). Similar to thymine, the lowest energy tautomer of uracil is the diketo form and the second lowest tautomer is an enol form, lying 46.35 kJ/mol higher than the diketo tautomer according to high level ab initio calculations [134]. In all, 13 tautomers are identified in the work presented in [134], with relative energies up to 131 kJ/mol compared to the lowest lying diketo form. The room temperature PE spectrum of uracil thus consists of the contribution of a unique tautomer, for instance the diketo one. Experimentally, the adiabatic ionization energy of uracil was measured to be AIE $= 9.15 \pm 0.03$ eV [37], which is slightly higher than thymine's AIE. We can also mention the electron impact ionization value of VIE $= 9.59 \pm 0.08$ eV [33], in excellent agreement with the PES value obtained by Kubota et al. [21].

4.2.3 Adenine

The most stable tautomer of adenine is 9H-adenine, followed by two other tautomers, i.e., 3H-adenine and 7H-adenine at energies of 29 and 31 kJ/mol with respect to 9H-adenine. Both theoretical and experimental studies demonstrated that gas-phase adenine produced by heating and then followed by jet-cooling leads efficiently to the predominance of the 9H-adenine isomer in gas phase prior to ionization [43, 137–142]. Hence, the photoionization experimental spectra were fully assigned to the single tautomer 9H-adenine$^+$ + e$^-$ ← 9H-adenine + $h\nu$ transition.

The ionization of adenine has been widely studied since the 1970s using ultraviolet photoelectron spectroscopy [18, 20, 23, 143–145], photoionization mass spectrometry [146], electron impact mass spectrometry [28], and very

Fig. 11 *Upper panel*: Differentiated PIE (*black line*) [43] and PES spectrum (*green line*) [23] of adenine. *Lower panel*: Vertical ionization energies and the corresponding MOs as computed at the EOM-IP-CCSD/cc-pVTZ level by Bravaya et al. [43]. Reprinted with permission from Bravaya et al. [43]. Copyright (2010) American Chemical Society
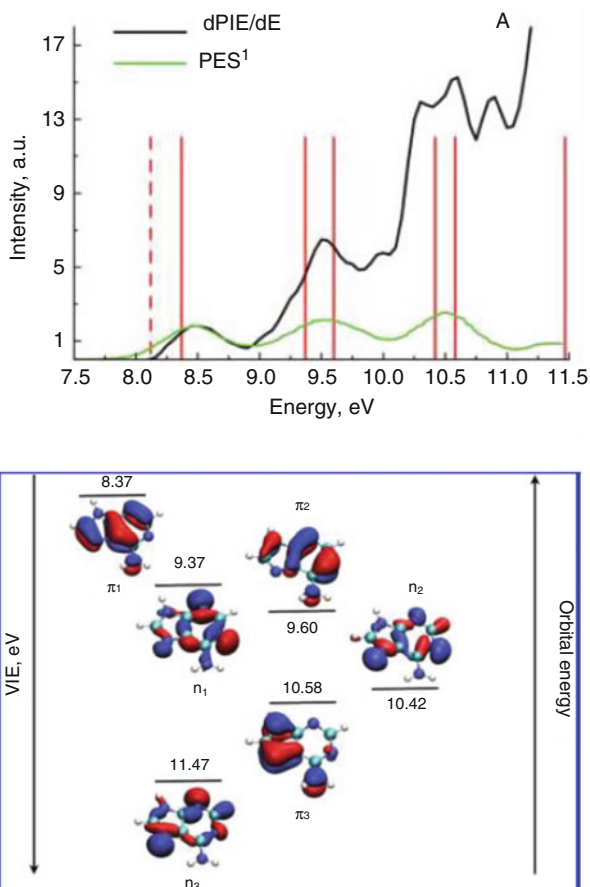
recently using slow photoelectron spectroscopy [11]. In the latter study, the close to zero kinetic energy photoelectrons and the corresponding photoions were measured in coincidence. The assignment of these experimental spectra was based on deep theoretical investigations of the structure and the electronic states of ionized adenine by means of modern theoretical methodologies [43, 147–150].

Below 8 eV, the experimental spectra of adenine present no signal and then the signals increase above $h\nu = 8$ eV [20, 23, 37, 43, 144]. This is exemplified in Fig. 11 where we show the PES spectrum of adenine measured by [23], the experimental dPIE/dE spectrum recorded at the Advanced Light Source, together with VIE calculations of [43] in the 7.5–11.5 eV energy range. Jochims et al. [37] used PIMS and SR from the BESSY synchrotron facility (Berlin-Adlershof) and proved that the fragmentation of the 9H-adenine[+] cation occurs for photon energies well above 11 eV. In 2013, this is confirmed by the threshold electron-ion coincidence measurements by Touboul et al. [11]. Therefore, the major contribution to the

photoelectron spectra in the energy range 8–11 eV corresponds to the 9H-adenine$^+$ radical cation.

In 2010, Krylov and coworkers computed an adiabatic ionization energy of adenine of AIE = 8.13 eV using the equation-of-motion coupled-cluster method [43]. This value agrees well with the onset of their PIE curve found at 8.20 ± 0.05 eV [43] (Fig. 11, upper panel). The TPEPICO spectrum of adenine [11] shown in Fig. 12 presents a sharp peak at threshold, which is attributed by Touboul et al. to the 9H-adenine$^+$ $\widetilde{X}0_0^0$ +e$^-$ ← 9H-adenine $\widetilde{X}0_0^0$ + $h\nu$ photoionization transition. This allowed them to determine accurately the adiabatic IE of 9H-adenine as AIE = 8.267 ± 0.005 eV. This value is in excellent agreement with previous ones obtained by photoionization mass spectrometry (PIMS) measurements of the relative intensity of the parent ion vs the photon energy (8.20 ± 0.03 eV [37]; 8.26 eV [146]). The vertical ionization energy (VIE) of 9H-adenine corresponds to the maximum of the first band in the photoelectron spectra and was measured to be VIE = 8.606 ± 0.006 eV [142], 8.44 ± 0.03 eV [143], and 8.48 eV [144] using photoionization techniques. The experimental VIE value of Nir et al. [142] is in excellent agreement with the maximum of the first electronic band of the TPEPICO spectrum shown in Fig. 12 (lower panel) [11]. The VIE is ~0.3 eV higher than the AIE. As established theoretically [43, 69, 151–153], this corresponds well to the Franck–Condon transition shift. Indeed, the geometrical changes between neutral and ionic 9H-adenine take place mainly on bond length and in-plane angles. In particular, ionized adenine does not lose its planarity. These precise ionization energies were used by Touboul et al. [11] to deduce an accurate heat of formation of the adenine radical cation $\Delta_f H_{298}$(adenine cation) of 1004 ± 9 kJ/mol. The photoionization mechanism close to and above the IEs is found to occur mainly via direct processes (Fig. 12). For the sake of completeness we mention that the IE values determined by electron impact ionization are less accurate and spread over 1 eV range [29, 154, 155].

In the 8–11 eV energy range, similar experimental spectra were measured for adenine as illustrated in Figs. 11, 12, and 13. They consist of broad bands due to the complex electronic structure of the cationic species. One can identify three broad bands centered at 8.6, 9.6, and 10.5 eV, respectively. These bands are structureless. Figure 11 displays the VIEs and the corresponding MOs as computed at the EOM-IP-CCSD/cc-pVTZ level by Krylov and coworkers [43]. According to these high level computations, these bands correspond to Koopmans-like ionization processes, where the first band is due to the ionization of the π-type HOMO, and the second and third bands are for the ionization from π- and σ-like molecular orbitals. In contrast to thymine and to the NAB analogues, the experimental spectra do not show any resolved vibrational structure in despite of a high enough experimental resolution. This is due to the complex electronic structure of 9H-adenine$^+$ as discussed widely by Krylov and coworkers [43]. For photon energies ≥11 eV, the PE spectrum (Fig. 13) is composed of several bands that were attributed to the ionization from the outer-valence orbitals of adenine. The corresponding vertical
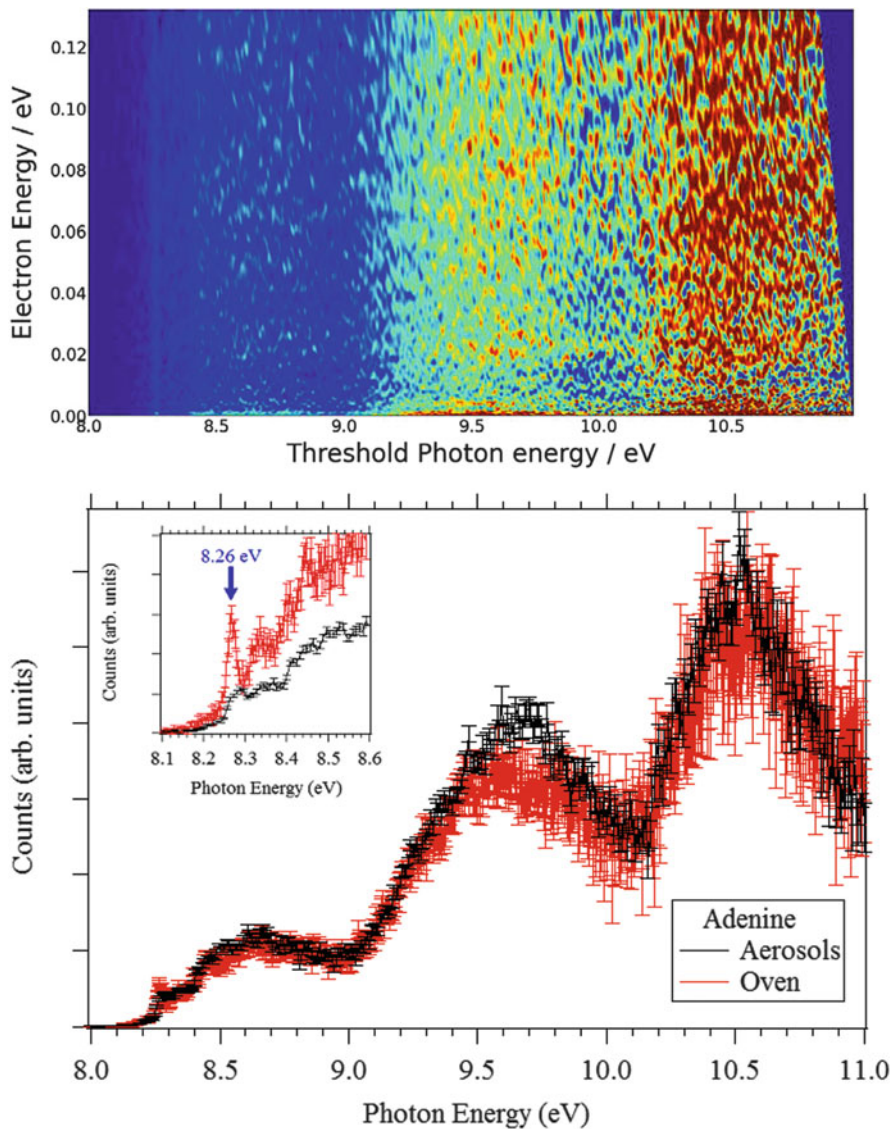
Fig. 12 *Upper panel*: Full scale 2D spectrum of adenine obtained using oven vaporization providing the photo-electron kinetic energies as a function of the photon energy. *Lower panel*: TPEPICO spectra of the adenine parent obtained with 40 meV threshold electron resolution. The *black curve* is when adenine is vaporized with the aerosol source and the *red curve* is for in-vacuum oven. The *inset* presents an energy close up of the threshold region. Reprinted with permission from Touboul et al. [11]. Copyright (2013), AIP Publishing LLC
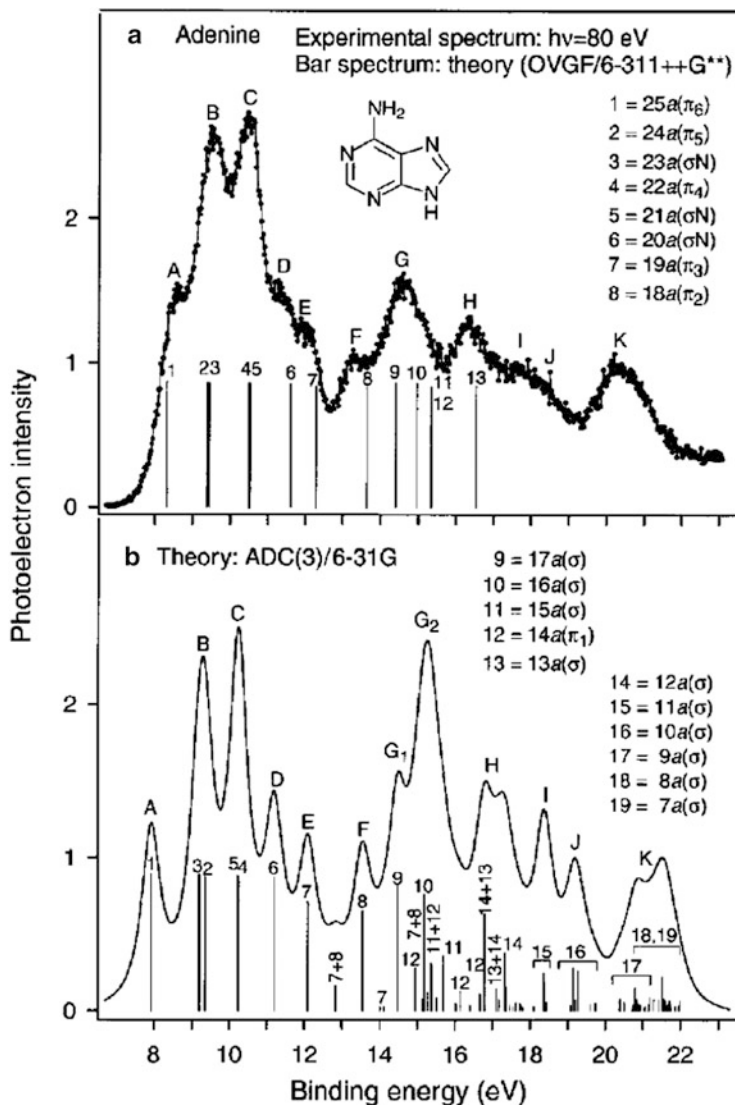
Fig. 13 *Upper panel*: Photoelectron spectrum of adenine recorded for $h\nu = 80$ eV. *Lower panel*: synthetic theoretical spectrum obtained using the ADC(3) method Trofimov et al. [23] © IOP Publishing. Reproduced with permission. All rights reserved

ionization energies are listed in [23]. Some of the associated bands overlap significantly. This participates to the congestion of the experimental spectra.

The VUV photochemistry of adenine is very complex. For instance, Leach and coworkers [37, 156], who used a quadrupole mass spectrometer and VUV-SR for a PIMS study of adenine in the range of 6–22 eV, were able, with the help of

thermochemical data, to deduce dissociative ionization mechanisms in detail. The recent experiments of Pilling et al. [157], using a photoelectron-photoion coincidence technique (PEPICO), confirmed such a complex chemistry upon ionization of adenine. Both groups showed that the adenine cation fragments at energies between 10.7 and 22 eV. However, the most abundant ion, even at $h\nu = 21$ eV, is still the parent ion $C_5H_5N_5^+$. This confirms the high stability of adenine upon absorption of a VUV photon. Both groups also observed other intense fragment ions such as $C_4H_4N_4^+$, $C_3H_3N_3^+$, $C_2H_2N_2^+$ (corresponding to successive losses of HCN), NH_2CNH^+, as well as $HCNH^+$. Through the analysis of the relative abundances for each ionic fragment and their mean kinetic energy release, they found that the production of the neutral HCN fragment represents up to 40% of the dissociative channels for this molecule as induced by VUV photons. Interestingly, some of these products are also observed after unimolecular decomposition of the δ-valerolactam cation as illustrated above.

4.2.4 Cytosine

In the literature there exist several ab initio computations of the equilibrium structures, the relative energies, and the ionization energies of the tautomers of cytosine [36, 42, 43]. These studies showed that these tautomers are close in energy. Five of them (for instance, C1, C2a, C2b, C3a, and C3b) are located within energy differences less than 11.5 kJ/mol (cf. Fig. 14). Accordingly, molecular beams of cytosine are most likely composed of a mixture of several tautomers prior to ionization. The composition of the neutral gas depends strongly on the techniques used for vaporization (gas temperature, oven vaporization, aerosols, etc., see our discussion in Sect. 2.3.1). The three most stable forms (for instance C1, C2b, and C3a) are expected to prevail. Analysis of the recent experimental photoionization spectra mainly considers the contribution of these three tautomers. This makes the situation more complicated for cytosine than for adenine.

Photoionization of cytosine was studied using mass spectrometry coupled to VUV rare gas lamps for excitation [39] and VUV-SR sources at the Advanced Light Source [38, 42], at the Daresbury Laboratory storage ring [23], and very recently at Synchrotron SOLEIL [11]. The 2D spectrum of the cytosine$^+$ cation, of photoelectrons having kinetic energies from 0 to 140 meV is displayed in Fig. 15 (upper panel) [11]. This 2D matrix reveals that the single photoionization of cytosine occurs mainly by a direct process in the energy ranges of interest, so that autoionization processes can be neglected. We present in Fig. 14 the PES and the differentiated PIE curve (upper panel) up to 3 eV above the IE and in Fig. 15 (lower panel) the TPEPICO spectrum of cytosine from threshold up to 2 eV above the IE. This is the spectral region covering the excitation of the lowest lying electronic excited states of the ion. Within the TPEPICO measurement scheme, the mass selection ensures that only the photoelectrons associated with the cytosine ion are detected in coincidence, ruling out the contribution of eventual fragments. All these experimental spectra are similar. They start by a sharp increase of the signal close to the IE of cytosine.
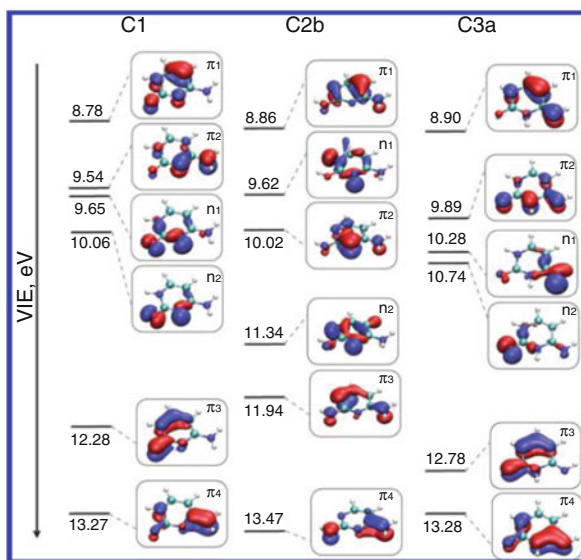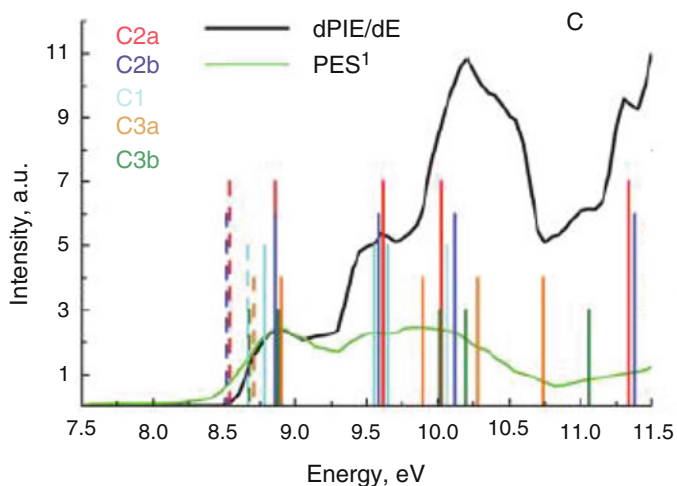
Fig. 14 *Upper panel*: Differentiated experimental PIE spectrum (*black line*) of cytosine [43] and experimental PES spectrum (*green line*) [23] of cytosine. *Lower panel*: Vertical ionization energies and the corresponding MOs as computed at the EOM-IP-CCSD/cc-pVTZ level by Krylov and coworkers [43]. C1, C2b, and C3a correspond to the most stable forms of the neutral cytosine. See [23] for more details. Reprinted with permission from Bravaya et al. [43]. Copyright (2010) American Chemical Society

The ionization energy of cytosine has been determined experimentally by several methods. Using electron impact ionization, the IE is found to be IE $= 9.0 \pm 0.1$ eV [154]. Using PIMS in combination with a hydrogen discharge lamp, values of AIE $= 8.68$ eV and VIE $= 8.94$ eV have been obtained [146]. With
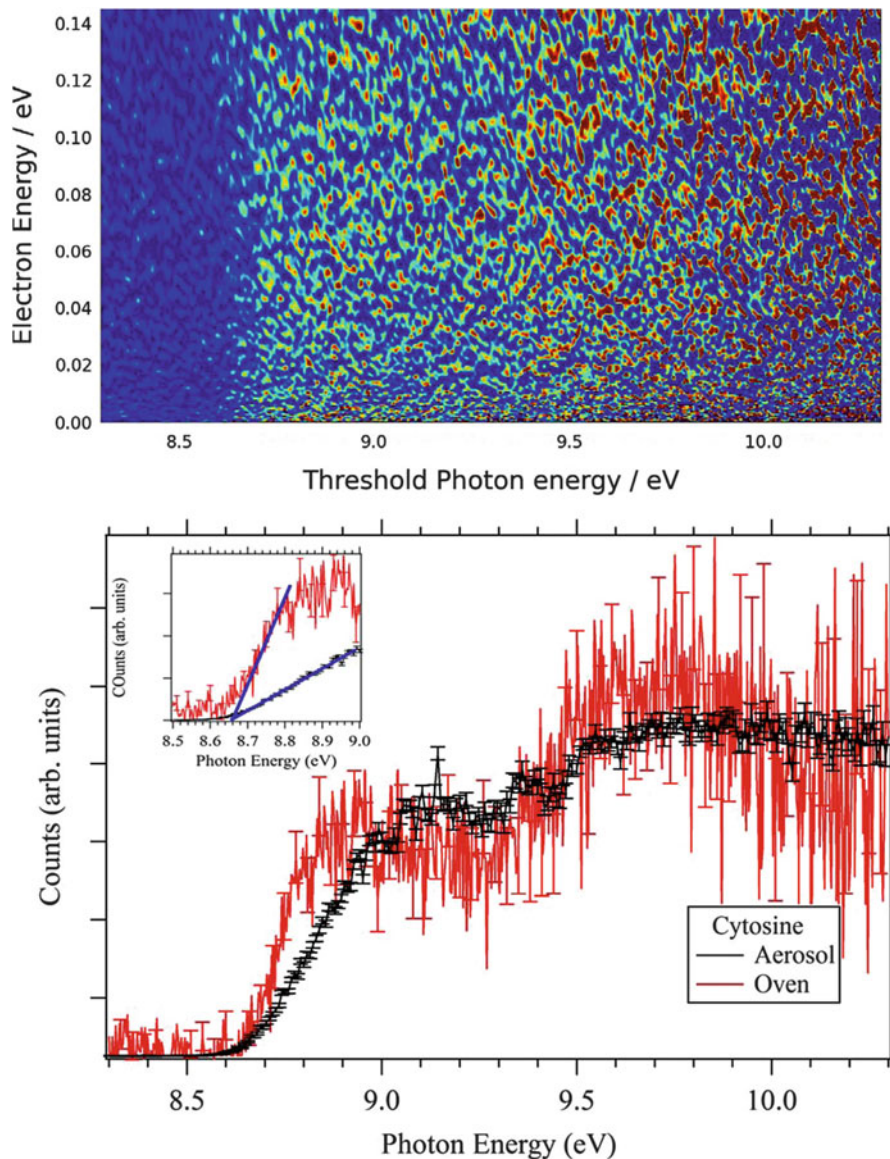
Fig. 15 *Upper panel*: Full scale 2D spectrum of cytosine obtained using oven vaporization providing the photo-electron kinetic energies vs the photon energy. *Lower panel*: TPEPICO spectra of the cytosine parent obtained with 40 meV threshold electron resolution when using the aerosol source (*black curve*) and with 80 meV (*red curve*) when using the in-vacuum oven. The *inset* is an enlargement for the threshold ionization energy where the *oblique lines* are to enlighten the slopes at the ionization threshold. Reprinted with permission from Touboul et al. [11]. Copyright (2013), AIP Publishing LLC

PES, IE = 8.45 eV [19] and VIE = 8.94 ± 0.03 eV [143] are obtained. Finally, very recently, the AIE of cytosine has been determined to be AIE = 8.66 ± 0.01 eV using TPEPICO [11]. Since there is no clear adiabatic transition in the TPEPICO spectrum of [11], the latter value was deduced by linear extrapolation of the first onset of the TPEPICO spectrum as illustrated in the inset in Fig. 15. This recent AIE value agrees very well with the measurements of Kostko et al. (8.60 ± 0.05 eV [42]), whereas some deviations are observed with the earlier PES values which can be partially explained by different compositions of the cytosine tautomer distribution in the gas jet prior to photoionization. The spectra are composed of several overlapped bands corresponding to the population of the ground and the first two electronic excited states of this cation. For energies >11 eV, the PE spectrum (Fig. 16) shows several bands due to ionization of the outer-valence molecular orbitals of cytosine.

Similar to adenine, the VUV photochemistry of cytosine upon ionization is complex. For illustration, we mention the combined theoretical and neutralization–reionization mass spectrometric study performed by Wolken et al. [36] (cf. Fig. 17). Interestingly, these authors observed that metastable cytosine cation–radicals undergo ring-cleavage dissociations by eliminations of CO (major) and HNCO (minor). The production of CO was also discussed for the fragmentation of thymine$^+$, 2-pyridone$^+$, and 2-hydroxypyridone$^+$ cations (see above).

4.2.5 Guanine

Guanine has been a little less studied in the past than the other biological NABs, most probably because it is more difficult to bring this compound into the gas phase as compared to the other NABs whose molecular weight is lower. The compound has to be heated up to more than 300°C, which is close to its melting point, in order to have sufficient vapor pressure to perform gas phase measurements. Using SR-PIMS, Zaytseva et al. showed that, even at these high temperatures, guanine is not thermally degraded [24]. Furthermore, guanine is insoluble in water, in contrast to all other biological NABs, which hinders the use of the soft aerosol desorption technique described above. PE spectra are presented in [19, 24]. In the article of Hush and Cheung [143], an ionization energy determined by PES is reported. Electron impact ionization studies are given in [28, 158]. Plekan et al. recorded PI mass spectra using rare gas lamp radiation at five spectral lines between 8.43 and 21.2 eV [39]. Jet-cooled guanine and G-(H$_2$O)$_n$ ($n = 1$–3) clusters have also been studied at the Advanced Light Source, using PIMS [38, 41]. The most comprehensive theoretical studies of higher excited states of neutral and ionic guanine are detailed in [24, 147, 148, 159]. Briefly, they mainly concern the simulations of its PE spectrum [24], ab initio calculations of the ionization energies [147, 148] and of the relative energies of the numerous guanine tautomers [159].

Guanine has four nitrogen-bonded hydrogen atoms that can potentially migrate. According to the ab initio calculations presented in [159], the four lowest lying tautomers are within 0.1 eV of each other. Four other tautomers lie within 0.28 eV
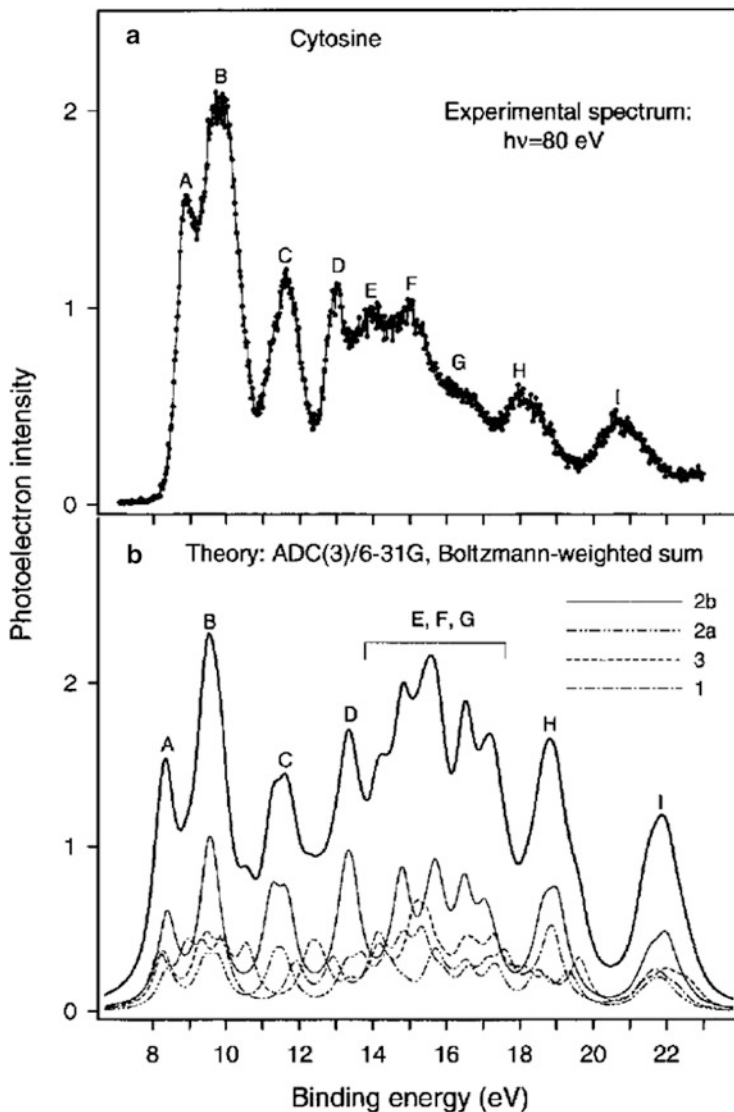
Fig. 16 *Upper panel*: Photoelectron spectrum of cytosine recorded for $h\nu = 80$ eV. *Lower panel*: synthetic theoretical spectrum obtained using the ADC(3) method (Trofimov et al. [23]) © IOP Publishing. Reproduced with permission. All rights reserved

above the lowest. Gas phase guanine, even if jet-cooled, is therefore necessarily a mixture of these different molecules. According to IE calculations reviewed in [41], their respective AIEs lie between 7.80 and 8.17 eV, and their VIEs between 8.16 and 8.44 eV. These values agree well with experimental PE spectra [19, 24]. Zhou et al. [41] tried to relate the experimental photoionization efficiency curve recorded
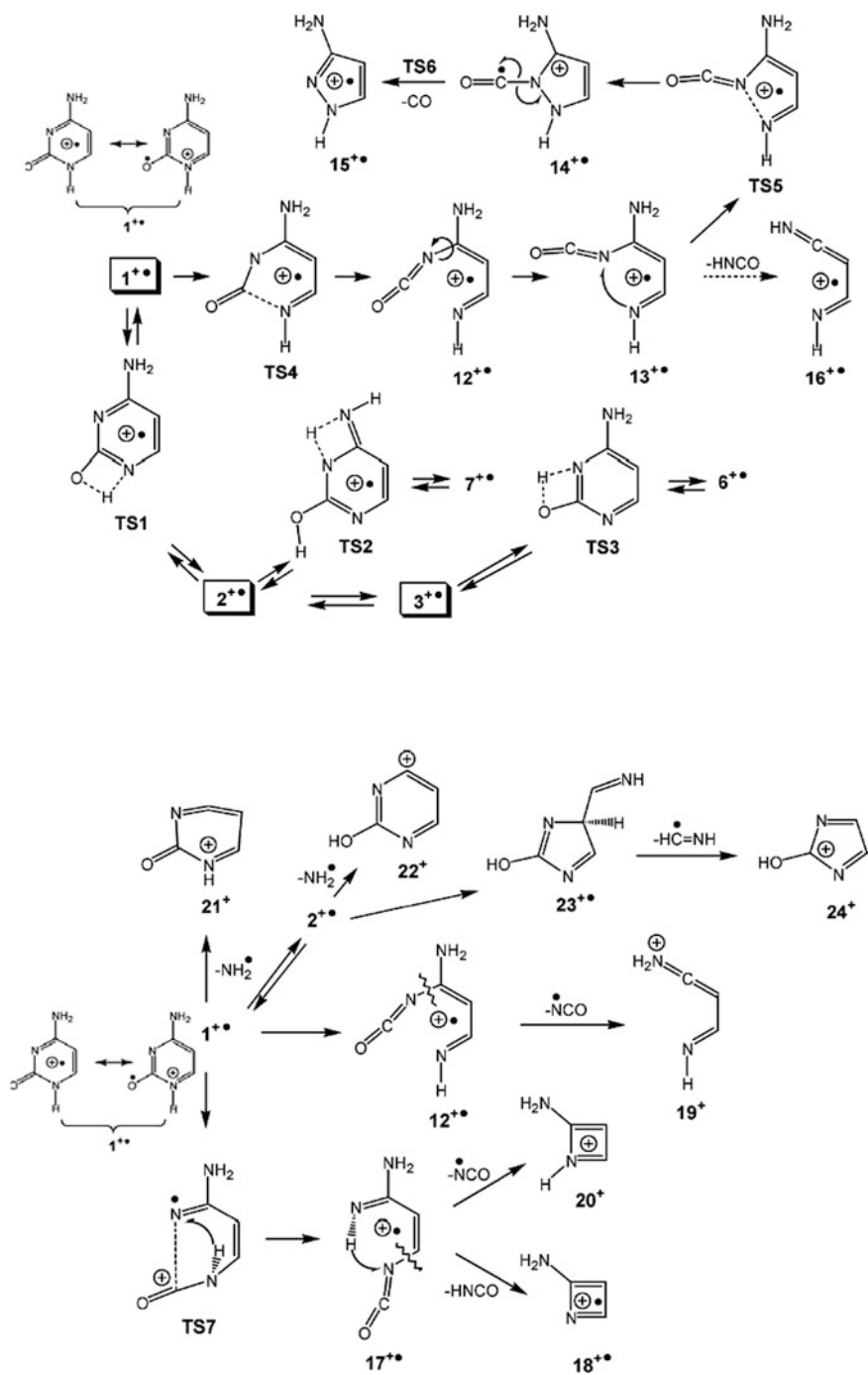
Fig. 17 Schematic representation of the unimolecular decomposition processes undertaken by the cytosine⁺radical cation. Reprinted from Wolken et al. [36] Copyright (2007), with permission from Elsevier

by PIMS in combination with VUV-SR to the theoretical VIEs. Comparing thermal vaporization and laser desorption by an Nd:YLF laser (operating at $\lambda = 527$ nm), they were able to show that different tautomer populations are produced with these two different vaporization methods. In the comprehensive theoretical and experimental study of Zaytseva et al. [24], full valence shell PE spectra from the IE up to 24 eV are presented. In their calculations, the four most stable guanine tautomers are considered. The composite theoretical spectrum, constructed from a Boltzmann distribution of the four tautomers at $T = 600$ K, reproduces the experimental PE spectrum quite well (see Fig. 18).

The dissociative photoionization of guanine has been studied by Plekan et al. [39], using rare gas lines for excitation and time-of-flight PIMS, at 8.43, 10.0, 11.62, 16.67, and 21.2 eV incident photon energies. These authors measured a dominating mass peak corresponding to the parent ion of guanine, $C_5H_5N_5O^+$, for all photon energies (even at 21.2 eV). Similar to adenine$^+$, the guanine$^+$ cation shows a remarkable stability against VUV radiation-induced fragmentation. For $h\nu = 11.62$ eV the PI mass spectrum of guanine is almost fragment-free. Fragmentation develops at higher energies. At $h\nu = 21.2$ eV the main fragment ions are m/z 43 and 44, which have, however, less than half the intensity of the parent ion. Many other ions with low intensity are also observed. For the sake of completeness, we mention the earlier EI mass spectrometric studies [28, 158]. Rice and Dudek [28] have made suggestions for fragmentation mechanisms of guanine (and three different methyl derivatives) upon electron impact ionization. However, a detailed study of the photoionization fragmentation mechanisms, taking advantage of accurate thermochemical data of the implied cationic and neutral fragments, is still missing. Nowadays, such thermochemical data can be calculated in a relatively easy way.

4.3 Complexes of NABs

The investigation of NABs complexes of increasing size can mimic the transition from the isolated molecules to the solution (or bulk) phase. For instance, the microhydration of the NABs T, A, C, and G has been studied recently at the Advanced Light Source [38, 44]. The experimental PIE spectra of mono-, di-, and tri-hydrates are used to gain insight into the computation of the FCF of such hydrogen-bonded aggregates. These authors found that ionization energies of mixed NAB-$(H_2O)_n$ ($n = 1$–3) clusters decrease by 0.3 eV approximately when going from $n = 0$ to $n = 3$, except for guanine. For the latter, the onset of the PIE curve of the monomer $C_5H_5N_5O^+$ is found at $E = 8.1 \pm 0.1$ eV (see our discussion above). The onsets of the PIE curves of the three water clusters G-$(H_2O)_n$ ($n = 1$–3) are all found at 8.0 ± 0.1 eV, indicating that the shift in ionization energy upon microhydration is only about 0.1 eV for this molecule. However, one must note the poor signal-to-noise ratio of the G-$(H_2O)_n$ ($n = 1$–3) PIE curves in these difficult experiments. In a related topic, the combined theoretical and SPES studies of the
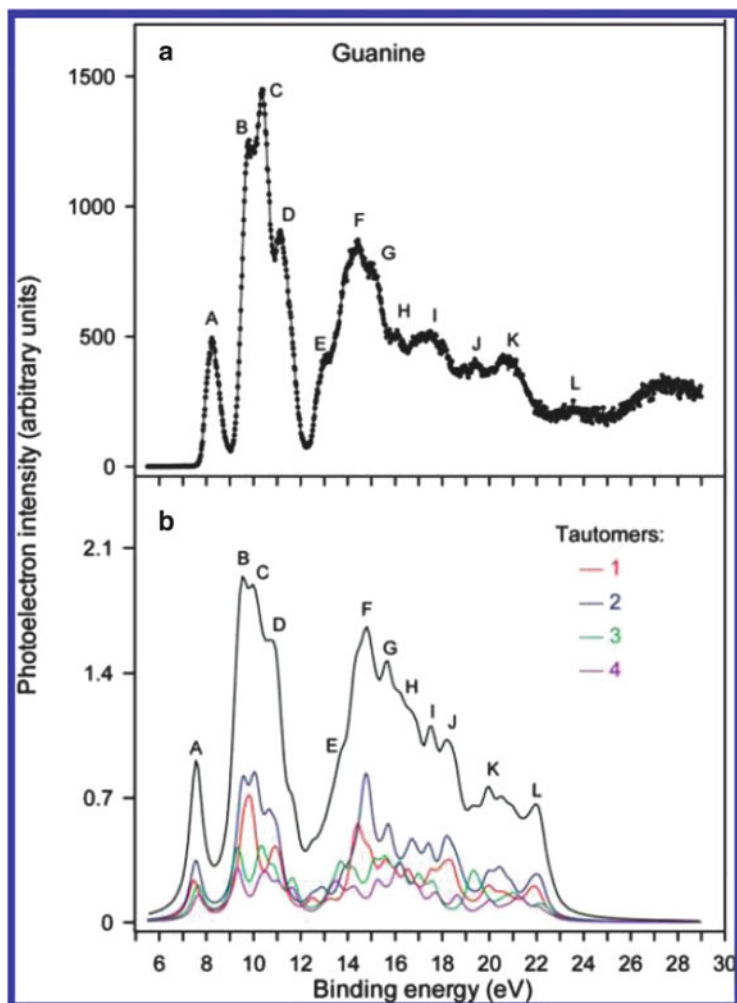
Fig. 18 (**a**) Experimental valence shell photoelectron spectrum of guanine, photon energy 100 eV. (**b**) Composite theoretical spectrum of guanine, constructed from the Boltzmann-weighted sum for $T = 600$ K of the individual spectra representing the 1–4 forms. The individual contributions are also shown. Reprinted with permission from Zaytseva et al. [24]. Copyright (2009) American Chemical Society

δ-valerolactam dimer [95, 97] revealed that (δ-valerolactam)$_2^+$ cation is subject to an intramolecular isomerization, H-transfer, and further unimolecular fragmentation processes. These unimolecular processes occur either along the ground or the excited state potential energy surfaces of (δ-valerolactam)$_2^+$.

Thymine dimers and the binary adenine–thymine aggregate have also been thoroughly studied, both experimentally and theoretically. For instance, theoretical binding energies (between monomers in the dimer) of different geometries and the

computed AIEs and VIEs of these aggregates are reported and analyzed in [12]. It was found there that the non-covalent interactions strongly affect the ionization energies, both AIE and VIE. The origin of the experimental PIE curve agrees well with the calculated AIE of a π-stacked TT dimer. The observed IE shifts in AA and AT clusters are smaller relative to TT, probably due to a less efficient overlap of the highest molecular orbitals, the smaller dipole of A, and the larger energy gap between ionized states of A and T monomers in the case of AT.

5   Conclusions and Perspectives

The present chapter reviews the most recent theoretical and experimental methodologies and results on the photoionization of NABs and their analogues in the VUV spectral regime. The electron spectroscopy of the ions and their unimolecular decomposition processes were mainly covered. It turns out from this presentation that the complexity of the spectra is due to the complex electronic structure of the cationic species and to the possible contribution of more than one tautomer. Thymine apparently represents an exception with a vibrationally resolved spectrum. The fragmentation of NAB cations leads to the formation of CO, HCN, and other prebiotic units. As stated above, the reverse reactions in prebiotic media may be at the origin of the formation of biological building blocks in these media.

In the field of theoretical chemistry, new developments for treating the nuclear dynamics beyond the adiabatic approximation should be undertaken. Indeed, the experimental spectra of the NABs and of their analogues show strong vibronic coupling between the cationic electronic states. These couplings induce mixing of the electronic wave functions of the corresponding electronic states in the vicinity of their avoided crossings or crossing. Hence, they strongly disturb the pattern of rovibrational levels of these states and result in nontrivial nuclear dynamics. In this case, the system behavior can be revealed by time-dependent multidimensional wave packet simulations, while taking into account coupling between the electronic states, and so exploring the dynamics beyond the Born–Oppenheimer or adiabatic approximation. Such types of simulation are still challenging and should be developed. This is also essential for studying pairing between DNA base pairs and damage of the hydrogen bonding systems by X-ray radiation.

The interaction of DNA and RNA bases and analogs with soft and hard X-ray light can result in ultrafast physico-chemical processes more complex than direct photoionization. These ultrafast processes induced by core-hole or valence ionization may also be studied in the near future. Inner-shell excitation or ionization of isolated molecules leads to the formation of highly excited species, which have been shown to decay on a very short timescale (order of femtosecond) by electronic decay and/or nuclear motion or dissociation. Following the excitation or ionization of electrons from the K (1s), L (2p), or M (3d) electronic shells of light elements constituting the DNA bases (C, N, O), electronic decay of the system will most probably occur (~99% of the decay events) by non-radiative electronic decay

(so called Auger decay), producing ions in a broad range of excited electronic and rovibrational states. The resonant processes form single charged cations, while non-resonant inner-shell ionization results in the formation of dications. The cross-sections for these channels depend on the frequency of the X-ray radiation, on transition dipole moments, as well as on the potential energy surface of the core-hole and cationic states. These scattering processes are described essentially as one-step processes. They may result in unusual molecular decomposition, ultrafast dissociation, or unexpected molecular reactivity, and have to be taken into account in order to obtain the global picture of photo-induced reaction and damage of the DNA base prototypes. Investigation of these processes can be done with the help of time-dependent wave packet scattering through intermediate core-hole states and, experimentally, by X-FEL sources.

From an experimental point of view, different vaporization methods have been applied to study gas phase NABs. They all proved to be successful. Their respective advantages and disadvantages have been discussed in this chapter. Their efficiency will probably be further enhanced in the future but substantial progress (by orders of magnitude) is currently not expected from this side. Concerning VUV beamlines coupled to third generation VUV-SR sources, we are today probably close to the limit to what can be done in terms of experimental spectroscopy of NABs with these sources, in combination with the connected state-of-the-art ion and electron spectrometers (considering for instance the problem of spectral congestion). In the field of experimental molecular VUV photophysics, a promising new step is the advent of VUV FEL sources developed in parallel at several places in the world (Germany, Italy, China, USA), with brilliances well above third generation SR sources. Although the tunability of these sources will be limited (in the beginning), their pulsed time structure will allow (1) for pump-probe spectroscopy well above the ionization threshold and (2) the straightforward combination with pulsed laser desorption. This will open up a whole new research field of experimental and theoretical VUV photophysics.

References

1. Hagen U (1986) Radiat Environ Biophys 25:261
2. Kumar A, Sevilla MD (2010) Chem Rev 110:7002
3. Shikazono N, Noguchi M, Fujii K, Urushibara A, Yokoya A (2009) J Radiat Res 50:27
4. Ng CY (2014) Annu Rev Phys Chem 2014:65
5. Pan Y, Zhang L, Guo H, Deng L, Qi F (2010) Int Rev Phys Chem 29:369
6. Zhou Z, Guo H, Qi F (2011) Trends Anal Chem 30:1400
7. Bodi A, Hemberger P, Gerber T, Sztáray B (2012) Rev Sci Instr 83:083105
8. Garcia GA, Cunha de Miranda BK, Tia M, Daly S, Nahon L (2013) Rev Sci Instr 84:053112
9. Poully JC, Schermann JP, Nieuwjaer N, Lecomte F, Gégoire G, Desfrançois C, Garcia GA, Nahon L, Nandi D, Poisson L, Hochlaf M (2010) Phys Chem Chem Phys 12:3566
10. Gaie-Levrel F, Garcia GA, Schwell M, Nahon L (2011) Phys Chem Chem Phys 13:7024
11. Touboul D, Gaie-Levrel F, Garcia GA, Nahon L, Poisson L, Schwell M, Hochlaf M (2013) J Chem Phys 138:094203
12. Bravaya BS, Kostko O, Ahmed M, Krylov AI (2010) Phys Chem Chem Phys 12:2292
13. Golan A, Bravaya KB, Kudirka R, Kostko O, Leone SR, Krylov AI, Ahmed M (2012) Nat Chem 4:323
14. Golan A, Ahmed M (2012) J Vis Exp 68:e50164
15. Lauer G, Schäfer WW, Schweig A (1975) Tetrahedron Lett 45:3942
16. Dougherty D, Wittel K, Meeks J, McGlynn SP (1976) J Am Chem Soc 98:3815
17. Padva A, O'Donnell TJ, LeBreton PR (1976) Chem Phys Lett 41:278
18. Peng S, Padva A, LeBreton PR (1976) Proc Natl Acad Sci USA 73:2966
19. Dougherty D, Younathan ES, Voll S, Abdulnur S, McGlynn SP (1978) J Electron Spectrosc Relat Phenom 13:379
20. Urano S, Yang X, LeBreton PR (1989) J Mol Struct 214:315
21. Kubota M, Kobayashi T (1996) J Electron Spectrosc Relat Phenom 82:61
22. Dolgounitcheva O, Zakrzewski VG, Ortiz JV (2002) J Phys Chem A 106:8411
23. Trofimov AB, Schirmer J, Kobychev VB, Potts AW, Holland DMP, Karlsson L (2006) J Phys B At Mol Opt Phys 39:305
24. Zaytseva IL, Trofimov AB, Schirmer J, Plekan O, Feyer V, Richter R, Coreno M, Prince KC (2009) J Phys Chem A 113:15142
25. Müller-Dethlefs K, Schlag EW (1998) Angew Chem Int Ed 37:1346
26. Leach S, Eland JHD, Price SD (1989) J Phys Chem 93:7575
27. Rice JM, Dudek GO, Barber M (1965) J Am Chem Soc 87:4569
28. Rice JM, Dudek GO (1967) J Am Chem Soc 89:2719
29. Lifschitz C, Bergmann ED, Pullman B (1967) Tetrahedron Lett 46:4583
30. Ulrich J, Teoule R, Massot R, Cornu A (1969) Org Mass Spectrom 2:1183
31. Barrio MG, Scopes DIC, Holtwick JB, Leonard NJ (1981) Proc Natl Acad Sci USA 78:3986
32. Sethi SK, Gupta SP, Jenkins EE, Whitehead CW, Townsend LB, McCloskey JA (1982) J Am Chem Soc 104:3349
33. Denifl S, Sonnweber B, Hanel G, Scheier P, Märk TD (2004) Int J Mass Spectrom 238:47
34. Denifl S, Ptasińska S, Gstir B, Scheier P, Märk TD (2004) Int J Mass Spectrom 232:99
35. Turecek F, Wolken JK (2001) J Phys Chem A 105:8740
36. Wolken JK, Yao C, Turecek F, Polce MJ, Wesdemiotis C (2007) Int J Mass Spectrom 267:30
37. Jochims HW, Schwell M, Baugärtel H, Leach S (2005) Chem Phys 314:263
38. Belau L, Wilson KR, Leone SR, Ahmed M (2007) J Phys Chem A 111:7562
39. Plekan O, Feyer V, Richter R, Coreno M, de Simone M, Prince KC (2007) Chem Phys 334:53
40. Feyer V, Plekan O, Richter R, Coreno M, Prince KC (2009) Chem Phys 358:33
41. Zhou J, Kostko O, Nicolas C, Tang X, Belau L, de Vries MS, Ahmed M (2009) J Phys Chem A 113:4829
42. Kostko O, Bravaya KB, Krylov AI, Ahmed M (2010) Phys Chem Chem Phys 12:2860

43. Bravaya KB, Kostko O, Dolgikh S, Landau A, Ahmed M, Krylov AI (2010) J Phys Chem A 114:12305
44. Khistyaev K, Bravaya KB, Kamarchik E, Kostko O, Ahmed M, Krylov AI (2011) Faraday Discuss 150:313
45. Khistyaev K, Golan A, Bravaya KB, Kamarchik E, Orms N, Krylov AI, Ahmed M (2013) J Phys Chem A 117:6789
46. Mysak E, Wilson KR, Jiminez-Cruz M, Ahmed M, Baer T (2005) Anal Chem 77:5953
47. Wilson KR, Jiminez-Cruz M, Nicolas C, Belau L, Leone SR, Ahmed M (2006) J Phys Chem A 110:2106
48. Kostko O, Takahashi LK, Ahmed M (2011) Chem Asian J 6:3066
49. Gaie-Levrel F, Gutlé C, Jochims HW, Rühl E, Schwell M (2008) J Phys Chem A 112:5138
50. Leach S, Schwell M, Garcia GA, Benilan Y, Fray N, Gazeau MC, Gaie-Levrel F, Champion N, Guillemin JC (2013) J Chem Phys 139:184304
51. Baer T, Mayer PM (1997) J Am Soc Mass Spectrom 8:103–115
52. Briant M, Poisson L, Hochlaf M, de Pujo P, Gaveau MA, Soep B (2012) Phys Rev Lett 109:193401
53. Gaussian, Revision A, Frisch MJ, Trucks GW, Schlegel HB, Scuseria GE, Robb MA, Cheeseman JR Scalmani G, Barone V, Mennucci B, Petersson GA, Nakatsuji H, Caricato M, Li X, Hratchian HP, Izmaylov AF, Bloino J, Zheng G, Sonnenberg JL, Hada M, Ehara M, Toyota K, Fukuda R, Hasegawa J, Ishida M, Nakajima T, Honda Y, Kitao O, Nakai H, Vreven T, Montgomery JA Jr, Peralta JE, Ogliaro F, Bearpark M, Heyd JJ, Brothers E, Kudin KN, Staroverov VN, Kobayashi R, Normand J, Raghavachari K, Rendell A, Burant JC, Iyengar SS, Tomasi J, Cossi M, Rega N, Millam NJ, Klene M, Knox JE, Cross JB, Bakken V, Adamo C, Jaramillo J, Gomperts R, Stratmann RE, Yazyev O, Austin AJ, Cammi R, Pomelli C, Ochterski JW, Martin RL, Morokuma K, Zakrzewski VG, Voth GA, Salvador P, Dannenberg JJ, Dapprich S, Daniels AD, Farkas Ö, Foresman JB, Ortiz JV, Cioslowski J, Fox DJ (2009) Gaussian, Inc., Wallingford CT
54. Werner H-J, Knowles PJ, Knizia G, Manby FR, Schütz M, Celani P, Korona T, Lindh R, Mitrushenkov A, Rauhut G, Shamasundar KR, Adler TB, Amos RD, Bernhardsson A, Berning A, Cooper DL, Deegan MJO, Dobbyn AJ, Eckert F, Goll E, Hampel C, Hesselmann A, Hetzer G, Hrenar T, Jansen G, Köppl C, Liu Y, Lloyd AW, Mata RA, May AJ, McNicholas SJ, Meyer W, Mura ME, Nicklaß A, O'Neill DP, Palmieri P, Pflüger K, Pitzer R, Reiher M, Shiozaki T, Stoll H, Stone AJ, Tarroni R, Thorsteinsson T, Wang M, Wolf A. See http://www.molpro.net for more details (versions 2008, 2010 and 2012)
55. Karlström G, Lindh R, Malmqvist PA, Roos BO, Ryde U, Veryazov V, Widmark PO, Cossi M, Schimmelpfennig B, Neogrady P, Seijo L (2003) Comput Mater Sci 28:222
56. Schmidt MW, Baldridge KK, Boatz JA, Elbert ST, Gordon MS, Jensen JH, Koseki S, Matsunaga N, Nguyen KA, Su S, Windus TL, Dupuis M, Montgomery JA Jr (1993) J Comput Chem 14:1347
57. Ahlrichs R, Bar M, Haser M, Horn H, Kolmel C (1989) Chem Phys Lett 162:165
58. Lischka H, Shepard R, Shavitt I, Pitzer RM, Dallos M, Mueller T, Szalay PG, Brown FB, Ahlrichs R, Boehm HJ, Chang A, Comeau DC, Gdanitz R, Dachsel H, Ehrhardt C, Ernzerhof M, Hoechtl P, Irle S, Kedziora G, Kovar T, Parasuk V, Pepper MJM, Scharf P, Schiffer H, Schindler M, Schueler M, Seth M, Stahlberg EA, Zhao J-G, Yabushita S, Zhang Z, Barbatti M, Matsika S, Schuurmann M, Yarkony DR, Brozell SR, Beck EV, Blaudeau J-P (2006) COLUMBUS: an ab initio electronic structure program, release 5.9.1: www.univie.ac.at/columbus
59. Stanton JF, Gauss J, Watts JD, Lauderdale WJ, Bartlett RJ (1992) Int J Quantum Chem S 26:879
60. Pople JA, Krishnan R, Schlegel HB, Binkley JS (1978) Int J Quantum Chem XIV:545
61. Møller C, Plesset MS (1934) Phys Rev 46:618
62. Hampel C, Peterson K, Werner HJ (1992) Chem Phys Lett 190:1
63. Amos RD, Andrews JS, Handy NC, Knowles PJ (1991) Chem Phys Lett 185:256

64. Knowles PJ, Hampel C, Werner HJ (1993) J Chem Phys 99:5219
65. Knowles PJ, Hampel C, Werner HJ (2000) J Chem Phys 112:3106
66. Raghavachari K, Trucks GW, Pople JA, Head-Gordon M (1989) Chem Phys Lett 157:479
67. Parr RG, Yang W (1998) Density functional theory of atoms and molecules. Oxford University Press, New York
68. Chong DP (ed) (1995) Recent advances in density functional methods. World Scientific, Singapore, p 287
69. Improta R, Scalmani G, Barone B (2000) Int J Mass Spectrom 201:321
70. Adler TB, Knizia G, Werner HJ (2007) J Chem Phys 127:221106
71. Werner HJ, Knizia G, Manby FR (2011) Mol Phys 109:407
72. Knizia G, Adler TB, Werner HJ (2009) J Chem Phys 130:054104
73. Brites V, Hochlaf M (2009) J Phys Chem A 113:11107
74. Lique F, Klos J, Hochlaf M (2010) Phys Chem Chem Phys 12:15672
75. Rauhut G, Knizia G, Werner HJ (2009) J Chem Phys 130:054105
76. Hochlaf M (2013) Phys Chem Chem Phys 15:9967
77. Peterson KA, Adler TB, Werner HJ (2008) J Chem Phys 128:084102
78. Weigend FA (2002) Phys Chem Chem Phys 4:4285
79. Hättig C (2005) Phys Chem Chem Phys 7:59
80. Klopper W (2001) Mol Phys 99:481
81. Yousaf KE, Peterson KA (2008) Chem Phys 129:184108
82. Watts JD, Gauss J, Bartlett RJ (1993) J Chem Phys 98:8718
83. Peterson KA, Dunning TH (2002) J Chem Phys 117:10548
84. Dunning TH (1989) J Chem Phys 90:1007
85. Douglas M, Kroll NM (1974) Ann Phys 82:89
86. Jansen G, Hess BA (1989) Phys Rev A 39:6016
87. de Jong WA, Harrison RJ, Dixon DA (2001) J Chem Phys 114:48
88. Knowles PJ, Werner HJ (1985) Chem Phys Lett 115:259
89. Werner HJ, Knowles PJ (1985) J Chem Phys 82:5053
90. Werner HJ, Knowles PJ (1988) J Chem Phys 89:5803
91. Knowles PJ, Werner HJ (1988) Chem Phys Lett 145:514
92. Sobolewski AL, Adamowicz L (1996) J Phys Chem 100:3933
93. Sobolewski AL, Adamowicz L (1996) Chem Phys 213:193
94. Hammoutène D, Hochlaf M, Ciofini I, Adamo C (2010) Int J Quant Chem 110:498
95. Mahjoub A, Hochlaf M, Poisson L, Nieuwjaer N, Lecomte F, Schermann JP, Grégoire G, Manil B, Garcia GA, Nahon L (2011) ChemPhysChem 12:1822
96. Ben Messaouda M, Abderrabba M, Mahjoub A, Chambaud G, Hochlaf M (2012) Comput Theor Chem 990:94
97. Mahjoub A, Hochlaf M, Garcia GA, Nahon L, Poisson L (2012) J Phys Chem A 116:8706
98. Pan Y, Lau KC, Poisson L, Garcia GA, Nahon L, Hochlaf M (2013) J Phys Chem A 117:8095
99. Langhoff SR, Davidson ER (1974) Int J Quantum Chem 8:61
100. Finley J, Malmqvist P, Roos BO, Serrano-Andrès L (1998) Chem Phys Lett 288:299
101. Celani P, Stoll H, Werner HJ, Knowles PJ (2004) Mol Phys 102:2369
102. Celani P, Werner HJ (2003) J Chem Phys 119:5044
103. Hudock HR, Levine BG, Thompson AL, Satzger H, Townsend D, Gador N, Ullrich S, Stolow A, Martinez TJ (2007) J Phys Chem A 111:8500
104. Poisson L, Nandi D, Soep B, Hochlaf M, Boggio-Pasqua M, Mestdagh JM (2014) Phys Chem Chem Phys 16:581
105. Bauernschmitt R, Ahlrichs R (1996) Chem Phys Lett 256:454
106. Furche F, Ahlrichs R (2002) J Chem Phys 117:7433
107. von Niessen W, Schirmer J, Cederbaum LS (1984) Comput Phys Rep 1:57
108. Schirmer J, Cederbaum LS, Walter O (1983) Phys Rev A 28:1237
109. Schirmer J, Angonoa G (1989) J Chem Phys 91:1754

110. Potts AW, Holland DMP, Trofimov AB, Schirmer J, Karlsson L, Siegbahn K (2003) J Phys B At Mol Opt Phys 36:3129
111. Cederbaum LS, Domcke W, Schirmer J, von Niessen W (1986) Adv Chem Phys 65:115
112. Schirmer J, Cederbaum LS, Walter O (1983) Phys Rev A 28:1237
113. Mertins F, Schirmer J (1996) Phys Rev A53:2140
114. Schirmer J, Mertins F (1996) Int J Quantum Chem 58:329
115. Pieniazek PA, Arnstein SA, Bradforth SE, Krylov AI, Sherrill CD (2007) J Chem Phys 127:164110
116. Pal S, Rittby M, Bartlett RJ, Sinha D, Mukherjee D (1987) Chem Phys Lett 137:273
117. Stanton JF, Gauss J (1994) J Chem Phys 101:8938
118. Kamiya M, Hirata SJ (2006) Chem Phys 125:074111
119. Pieniazek PA, Bradforth SE, Krylov AI (2008) J Chem Phys 129:074104
120. Golubeva AA, Pieniazek PA, Krylov AI (2009) J Chem Phys 130:124113
121. Wei CY, Yu WS, Chou PT, Hung FT, Chang CP, Lin TC (1998) J Phys Chem B 102:1053
122. Ramos AF, Smedarchina Z, Zgierski MZ (2000) J Chem Phys 113:2662
123. Gerega A, Lapinski L, Nowak MJ, Furmanchuk A, Leszczynski J (2007) J Phys Chem A 111:4934
124. Garcia GA, Soldi-Lose H, Nahon L (2009) Rev Sci Instrum 80:023102
125. Trikoupis MA, Gerbaux P, Lavorato DJ, Flammang R, Terlouw JK (2002) Int J Mass Spectrom 217:1
126. Stefanovic D, Grutzmacher HF (1974) Org Mass Spectrom 9:1052
127. Cook MJ, El-Abbady S, Katritzky AR, Guimon C, Pfister-Guillouzo GJ (1977) Chem Soc Perkin Trans 2:1652
128. Trembreull R, Sin CH, Pang HM, Lubman DM (1985) Anal Chem 57:2911
129. Ozeki H, Cockett MCR, Okuyama K, Takahashi M, Kimura K (1995) J Phys Chem 99:8608
130. Lee D, Baek SJ, Choi KW, Choi YS, Kim SK (2002) Bull Korean Chem Soc 23:277
131. Potapov VK, Filyugina AD, Shigorin DN, Ozerova GA (1968) Dokl Akad Nauk SSSR 180:398
132. Treschanke L, Rademacher P (1985) J Mol Struct (Theochem) 122:35
133. Treschanke L, Rademacher P (1985) J Mol Struct 122:47
134. Rejnek J, Hanus M, Kabeláč M, Ryjáček F, Hobza P (2005) Phys Chem Chem Phys 7:2006
135. Choi KW, Lee JH, Kim SK (2005) J Am Chem Soc 127:15674
136. Majdi Y, Garcia GA, Nahon L, Schwell M, Poisson L, Hochlaf M Manuscript in preparation
137. Wang S, Schaefer HF III (2006) J Chem Phys 124:044303
138. Guerra CF, Bickelhaupt FM, Saha S, Wang F (2006) J Phys Chem A 110:4012
139. Hanus M, Kabelàc M, Rejnek J, Ryjacek F, Hobza P (2004) J Phys Chem B 108:2087
140. Piacenza M, Grimme S (2004) J Comput Chem 25:83
141. Plützer C, Nir E, de Vries MS, Kleinermanns K (2001) Phys Chem Chem Phys 3:5466
142. Nir E, Plützer C, Kleinermanns K, de Vries MS (2002) Eur Phys J D 20:317
143. Hush NS, Cheung AS (1975) Chem Phys Lett 34:11
144. Lin J, Yu C, Peng S, Akiyama I, Li L, Li KL, LeBreton PR (1980) J Am Chem Soc 102:4627
145. Satzger H, Townsend D, Stolow A (2006) Chem Phys Lett 430:144
146. Orlov VM, Smirnov AN, Varshavsky YM (1976) Tetrahedron Lett 17:4377
147. Roca-Sanjuan D, Rubio M, Merchan M, Serrano-Andrés LJ (2006) J Chem Phys 125:084302
148. Cauët E, Dehareng D, Liévin L (2006) J Phys Chem A 110:9200
149. Dolgounitcheva O, Zakrzewski VG, Ortiz JV (2000) Int J Quantum Chem 80:831
150. Dolgounitcheva O, Zakrzewski VG, Ortiz JV (2009) J Phys Chem A 113:14630
151. Colson AO, Besler B, Close DM, Sevilla MD (1992) J Phys Chem 96:661
152. Wetmore SD, Boyd RJ, Eriksson LA (1998) J Phys Chem B 102:10602
153. Reynisson J, Steenken S (2002) Phys Chem Chem Phys 4:527
154. Verkin BI, Sukodub LF, Yanson IK (1976) Dokl Akad Nauk SSSR 228:1452
155. Kim SK, Lee W, Herschbach DR (1996) J Phys Chem 100:7933
156. Schwell M, Jochims HW, Baumgärtel H, Dulieu F, Leach S (2006) Planet Space Sci 54:1073

157. Pilling S, Lago AF, Coutinho LH, de Castilho RB, de Souza GGB, Naves de Brito A (2007) Rapid Commun Mass Spectrom 21:3646
158. Zavilopulo AN, Shepnik OB, Agafanova AS (2009) J Phys B At Mol Opt Phys 42:025101
159. Hanus M, Ryjáček F, Kabeláč M, Kubar T, Bogdan TV, Trygubenko SA, Hobza P (2003) J Am Chem Soc 125:7678